International Journal of Heat and Mass Transfer 227 (2024) 125571

Contents lists available at ScienceDirect

International Journal of Heat and Mass Transfer

journal homepage: www.elsevier.com/locate/ijhmt

Experimental study on the influence of shell geometry and tube eccentricity on phase change material melting in shell and tube heat exchangers

Nazila Parsa [a], Babak Kamkari [b,*], Hossein Abolghasemi [a]

[a] Center for Separation Processes Modeling and Nano-Computations, School of Chemical Engineering, College of Engineering, University of Tehran, Tehran, Iran
[b] School of Engineering, Ulster University, Belfast, BT15 1AP, UK

ARTICLE INFO

Keywords:
Latent heat storage (LHS)
Shell geometry
Eccentricity
Phase change material (PCM)
Natural convection

ABSTRACT

This study experimentally investigates the combined effect of heat transfer fluid (HTF) tube eccentricity and shell geometry on the thermal performance of latent heat storage (LHS) units. Fifteen transparent shell and tube LHS units were designed and manufactured with circular, horizontal obround, and vertical obround shell geometries and various HTF tube eccentricities. All LHS units have an identical volume and were filled with paraffine as phase change material (PCM). By conducting visualization experiments, the effect of the HTF tube eccentricity (with values of 0, 0.2, 0.4, 0.6, and 0.8) on the thermal performance of LHS units was comprehensively analyzed. The melting process was photographed, and temperatures at predefined locations were recorded to determine the instantaneous liquid fractions and heat transfer characteristics of different systems. The findings revealed that the horizontal obround shell shortens the melting time compared to the traditional circular shell, while the vertical obround shell prolongs the melting time. It was observed that increasing the eccentricity factor from 0 to 0.8 leads to a reduction in melting time by up to 76 %, 72 %, and 60 % for vertical obround, circular, and horizontal obround shells, respectively, along with a substantial improvement of 304 %, 246 %, and 151 % in the time-averaged heat transfer rate. Moreover, the highest time-averaged heat transfer rate enhancements are achieved by the horizontal obround shell, which are 38 %, 77 %, 130 %, and 178 % for the eccentricity factors of 0, 0.2, 0.4, and 0.6, respectively, when compared with the concentric circular shell (base case). It has also been concluded that as the eccentricity factor increases from 0 to 0.8, the impact of the shell geometry on melting performance diminishes. At an eccentricity factor of 0.8, the difference in melting time among different geometries becomes negligible.

1. Introduction

In recent years, global energy consumption has significantly increased, leading to a heightened demand for energy derived from fossil fuels. As a result, the exorbitant prices of fossil fuels, the depletion of their reserves, and global warming resulting from greenhouse gas emissions are significant factors that continually motivate scientists to explore various potential methods of generating renewable energy sources [1–4]. Among all the renewable sources, solar energy stands out for its enormous potential to meet building heating and cooling demands, as well as to provide hot water for home and commercial use. However, due to the transient and intermittent nature of solar energy, an imbalance between energy supply and demand occurs. To address this issue, efficient energy storage systems need to be deployed [5–8]. Several thermal energy storage (TES) methods have been proposed to address the gap between energy supply and demand. These techniques include the utilization of sensible heat, latent heat, and thermochemical energy. Among these methods, the latent heat storage (LHS) approach employing phase change materials (PCMs) proves to be an attractive solution because of its capacity to store a significant amount of energy at a nearly constant operating temperature [9–11].

However, the primary limitation of many PCMs is their low thermal conductivity, which reduces the phase change rates during the melting and solidification process in latent heat thermal energy storage (LHTES) units. This challenge has motivated researchers to explore various techniques aimed at enhancing the performance of the phase change process in LHTES [12–14]. As a result, numerous effective heat transfer techniques have been employed to address this limitation, such as the insertion of fins [15–20], utilization of metal foam [21,22], use of wire mesh with high conductivity [23], implementation of heat pipe [24,25], utilization of multiple PCMs [26,27], incorporation of dispersed

* Corresponding author.
E-mail address: b.kamkari@ulster.ac.uk (B. Kamkari).

https://doi.org/10.1016/j.ijheatmasstransfer.2024.125571
Received 20 January 2024; Received in revised form 29 March 2024; Accepted 14 April 2024
Available online 24 April 2024

Nomenclature

A	heat transfer area (m^2)
A_h	cross-sectional area (m^2)
C_P	specific heat capacity (J/ kg.K)
D_h	hydraulic diameter (m)
ec	eccentricity
Fo	Fourier number
g	gravity acceleration (m/s^2)
h_{sl}	latent heat (J /kg)
k	thermal conductivity (W/m.K)
N	number of data
NP_0	number of pixels with 0 value
NP_t	total number of pixels
Nu	Nusselt number
$\overline{Nu}$	time-averaged Nusselt number
pH	wetted perimeter (m)
Q_{total}	total absorbed energy (J)
$\dot{Q}(t)$	heat transfer rate (J/s)
$\overline{\dot{Q}}$	time-averaged heat transfer rate (J/s)
Ra	Rayleigh number
Ste*	modified Stefan number
T	temperature (°C)
T_{m1}	onset of melting temperature (°C)
T_{m2}	endset of melting temperature (°C)
T_{mean}	mean temperature (°C)
t	time (s)
U	uncertainty
V	volume (m^3)
V_e	volume of enclosure (m^3)
x	independent variable

Abbreviation

DSC	Differential Scanning Calorimetry
EF	Elastomeric Foam
HTF	Heat Transfer Fluid
HX	Heat Exchanger
LHS	Latent Heat Storage
LHTES	Latent Heat Thermal Energy Storage
PCM	Phase Change Material
PID	Proportional-Integral-Derivative
RMSE	Root Mean Square Error

Greek symbols

γ	liquid fraction
∅	solid-liquid volume change
ρ	mass density (kg/m^3)
ν	kinematic viscosity (m^2/s)
α	thermal diffusivity (m^2/s)
β	thermal expansion coefficient (1/K)
θ	dimensionless temperature

Subscripts

a	apparent
exp	experiment
i	initial
l	liquid
m	melting
max	maximum
r	real
s	solid
w	wall

high-conductivity nanoparticles [28–30], encapsulation techniques [31], and ajustements in the enclosure inclination angle [11,32]. Moreover, the shell geometry, as well as the location and shape of the heat transfer tube, are other crucial aspects that affect the thermal performance of the shell and tube LHS units [33–41].

Alnakeeb et al. [33] numerically investigated the impact of various geometric parameters (eccentricity, aspect ratio, and heat transfer tube inclination) on the performance of a double-tube LHTES unit equipped with an inner elliptic tube for improving the melting properties of the PCM. According to their observations, increasing the eccentricity reduced the melting time for all aspect ratios. Moreover, a higher average melting rate was observed for larger eccentricity, as compared to a concentric configuration. Additionally, the results indicated that the inclination angle of the inner elliptic tube had a minimal impact on the melting process. In another numerical study conducted by Jain et al. [34], the melting dynamics of various LHS units with horizontally oriented cylindrical shell, and vertically oriented cylindrical and frustum shells were examined and compared. It was observed that the horizontal cylindrical shell and vertical frustum shell reduce the melting time by up to 34.21 % and 18.42 %, respectively, in comparison to the vertical cylindrical shell. Furthermore, in the horizontally oriented cylindrical shell, the eccentric inner tube enhances the rate of heat transfer and decreases melting time. Yazıcı et al. [35] developed an experimental study on the effect of inner tube eccentricity and inlet temperature of heat transfer fluid (HTF) on the melting behavior of paraffin in a horizontal tube-in-shell storage unit. It was concluded that the eccentric geometry significantly improves heat transfer inside PCM by intensifying natural convection. Furthermore, it was observed that the eccentric geometry (with the largest eccentricity) leads to a 67 % reduction in the total melting time compared to the concentric case. Safari et al. [36] conducted a numerical study to investigate the impact of various shell geometries (circle, vertical and horizontal rectangle, triangle, square, inverted triangle, and rhombus) and the inner tube eccentricity on the melting process of the PCM within shell and tube LHS units. The findings demonstrated that the heat exchanger (HX) featuring a circular shell with an eccentricity of 0.5 achieved a maximum reduction in melting time of 50.4 % compared to the base case, which involved a concentric circular shell. Pahamli et al. [37] conducted a numerical analysis to investigate the impact of different eccentricities of the inner tube, inlet temperature, and mass flow rate of HTF. The results indicated a 33 %, 57 %, and 64 % reduction in the duration of the melting process as the tube eccentricities increased to 0.25, 0.5, and 0.75, respectively. Additionally, increasing the Stefan number from 0.54 to 0.67 and 0.80 resulted in corresponding reductions in the duration of the melting process by 16 % and 27 %, respectively. Conversely, it was found that the Reynolds number did not significantly affect the melting time. Xu et al. [38] numerically investigated the melting performance of a horizontal shell and tube HX with an eccentric structure by employing porous-medium-enhanced PCM. The findings indicated that using an eccentric configuration and a porous medium can result in a 43.1 % reduction in the melting time. Additionally, it was concluded that the optimum eccentricity is directly proportional to the ratio of the outer and inner tube diameter, heating temperature, and porosity, while inversely proportional to thermal conductivity. Alnakeeb et al. [39] conducted a numerical analysis to investigate the effect of different eccentricities of the inner flat tube at different aspect ratios (1, 0.9, 0.8, 0.7, 0.6, and 0.5). The results indicated that, for all aspect ratios, the total melting time decreased as the eccentricity increased. It was also concluded that the highest melting rate occurred for the circular inner tube (aspect ratio= 1) with the largest eccentricity (0.75). Zheng et al.

Table 1
Variation of thermal conductivity of paraffin with temperature.

Temperature (°C)	20	30	40	50	60	65	70	75	80
Thermal conductivity (W/m.K)	0.202	0.2	0.199	0.198	0.145	0.143	0.142	0.139	0.138

Table 2
Thermophysical characterization of the paraffin and copper.

Materials	Copper	Paraffin
Melting temperature (°C)	–	54–56 (°C)
Density solid/liquid (kg/m^3)	8978	860/780
Thermal conductivity solid/liquid (W/m.K)	387.6	0.2/0.14
Viscosity (kg/m.s)	–	0.03
Specific heat solid/liquid (J/kg.K)	381	1820/2000
Thermal expansion coefficient, β (1/K)	–	0.0002
Latent heat (kJ*kg^{-1})	–	170

[40] performed a numerical study on the phase change processes of PCM in a shell and tube HX with varying eccentricities of the inner tube. Their findings indicate that eccentricity significantly impacts the melting time. Additionally, it was noted that an optimum eccentricity exists for minimizing the duration of both melting and solidification processes only when the Rayleigh number ratio exceeds 2.0. Dhaidan et al. [41] conducted experimental and numerical studies on the melting process of nano-enhanced PCMs within cylindrical shell and tube configurations, both concentric and eccentric. The findings indicated that the eccentric mode exhibits a higher melt fraction compared to the concentric arrangement. Furthermore, the addition of nanoparticles not only enhances the melting rate but also expedites the melting time, depending on the nanoparticle concentration.

After conducting a comprehensive literature review, it is evident that several studies have explored the influence of HTF tube eccentricity on the melting process of PCM within shell and tube LHS systems [35, 37–41]. In the effort to improve the heat transfer rate in LHS units, limited studies have investigated the influence of shell geometry on the melting process of PCM within horizontal shell-and-tube LHS systems [42,43]. Notably, investigations considering various shell shapes are scarce, and none have specifically focused on obround configurations. Additionally, much of the existing literature relies on numerical simulations, highlighting a critical gap that this current experimental work aims to tackle. To address these issues, this study experimentally visualizes the combined effect of the inner tube eccentricity and the shell geometries on the melting process and thermal performance of LHS systems. The melting process of PCM in both concentric and eccentric HXs with different shell geometries has been experimentally investigated. In addition to the circular shell selected as a base case for comparison, two other geometries, including horizontal and vertical obround shells, have been proposed while maintaining a constant mass of the PCM. A comparative study is conducted to analyze the thermal behavior of LHS units with varying HTF tube eccentricities and shell geometries. Experiments visualize the melting interface and record temperature history within PCM. Image processing and temperature data compute the liquid fraction, revealing a significant impact of HTF tube eccentricity on heat transfer rates and reducing melting times. These findings offer insights for shell and tube HX design, validating numerical models, and optimizing LHS units.

2. Experimental setup and procedure

2.1. Thermophysical properties of paraffin

The PCM utilized in the current study was 99 % pure paraffin supplied by Sigma-Aldrich Company. Paraffin is recognized as an ideal PCM for the storage of thermal energy in medium temperature applications, such as those used in solar and power plant exhaust systems, due to its broad melting temperature range [6,44]. To analyze the melting process, it is crucial to use differential scanning calorimetry (DSC) to measure the thermal characteristics of paraffin, such as the melting temperature range, latent heat, and specific heat capacity. The Decagon devices KD2 thermal analyzer, which has an accuracy of ±0.01 W/m °C, was employed to measure the thermal conductivity of paraffin in solid and liquid phases. The results, displayed in Table 1, outline the temperature-dependent thermal conductivity of paraffin. To determine the viscosity of the paraffin, a programmable viscometer (Model DVII+) was used. The density was measured using a Shimadzu analytical balance with an accuracy of ± 0.1 mg. Weighed paraffin was melted in an oven. The melted sample was put into $a \pm 1$ ml graduated cylinder and placed in a constant-temperature water bath. The liquid PCM density was determined by reading volume at various temperatures. Additionally, the density of the solid PCM was determined by cooling the melted PCM below the phase transition temperature. Table 2 lists the paraffin and copper tube's thermophysical characteristics. The average values of thermal conductivity for both the liquid and solid phases over the range of observed temperatures listed in Table 1 are shown in this table.

2.2. Experimental setup

An experimental setup was designed and constructed to assess the thermal performance of concentric and eccentric HXs with various shell geometries. A schematic diagram of the experimental setup, including a constant-temperature water bath with a proportional-integral-derivative (PID) controller, a digital camera, a flow meter, a temperature data logger, a circulation pump, a personal computer, and HX, is depicted in Fig. 1. The apparatus was designed to accurately measure the instant melt front and temperature within the PCM. Three different shell geometries (circular, horizontal, and vertical obround) with different eccentricities of HTF tube (0, 0.2, 0.4, 0.6, and 0.8) were used to examine the influence of HTF tube eccentricity in the different shell geometries on the thermal performance of PCM melting. For comparative purposes, the circular shell was chosen as the base case, while the obround enclosure was fabricated using a thermoforming process by heating and molding the circular shell in a pre-made mold. It is important to note that the volume of horizontal and vertical obround shells remains the same as that of the circular shell, implying that the mass of the enclosed PCM is the same in all enclosures. The shells were made of transparent Plexiglas, which allowed direct observation and photography of the melting phenomena while minimizing heat dissipation from the enclosure due to their low thermal conductivity ($k = 0.17$ W/m.K). The circular shell had dimensions of 120 mm in length and an inner and outer diameter of 90 and 100 mm, respectively. The water inlet and outlet were placed behind the HXs, leaving the front side accessible for photographing. The photographic views of the designed HXs are depicted in Fig. 2.

Two nested copper tubes, with diameters of 9 mm and 19.05 mm, were concentrically placed to transfer heat from the HTF to the PCM. Fig. 3 illustrates the flow of hot water entering the HX system through the inner tube inlet at a rate of 5 L/min. After passing through the inner tube, it flows in the opposite direction through the annular space between the two copper tubes. Upon exiting the system, the hot water returns to a constant-temperature bath controlled by a PID controller, maintaining hot water accuracy within ±0.1 °C. The nested tube configuration, combined with the high flow rate of HTF, minimizes the temperature differential between the input and output of HTF. This, along with the high thermal conductivity and thin wall of the copper tube, ensures a constant temperature across the outer surface of the

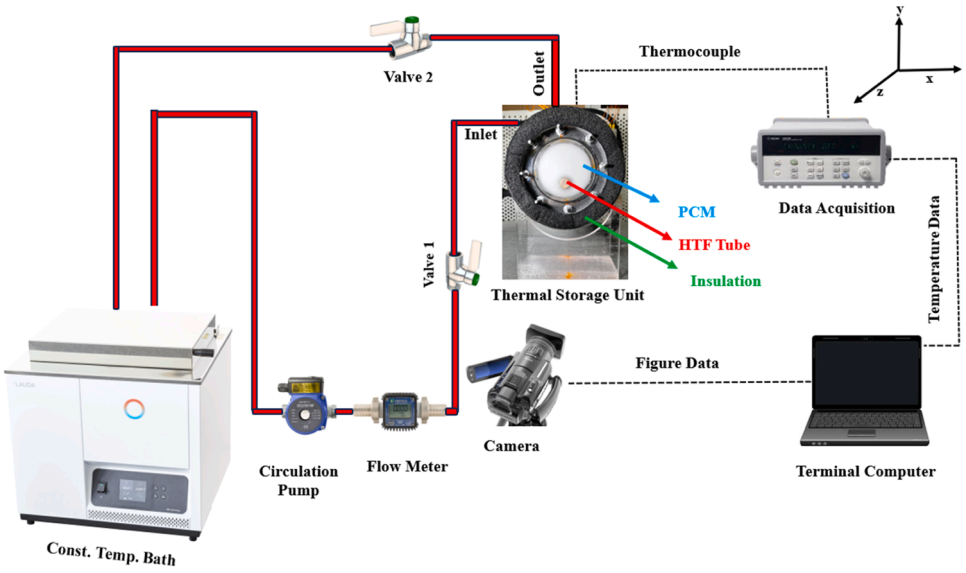

Fig. 1. Schematic diagram of the experimental apparatus.

inner tube, providing a consistent melting pattern along the HX axis. Therefore, the melting process can be considered two-dimensional, as the temperature difference along the axial direction of the HXs is negligible. The elastomeric foam (EF) insulation sheet ($K \leq 0.035$ W/m. K) with a thickness of 50 mm was used to insulate the HXs, with the aim of minimizing heat loss to the surroundings. The temperature of the HX's insulating surface was measured using an infrared thermometer to determine the amount of heat loss caused by the HX. During the melting process, the temperature variation between the insulation surface and the surrounding air was less than 1 °C. Due to this negligible temperature difference, the HX heat loss can be disregarded in the calculations.

To document the temperature history of the PCM at different locations, three holes were drilled around the shell, evenly spaced at 90° intervals. Four calibrated K-type thermocouples were inserted in the central part of the HX. To reduce flow disruption inside the enclosures, thermocouples with a small diameter are placed at just one cross-section of the HXs. The temperature changes were recorded using a temperature data logger. Fig. 4 shows the dimensions of the HXs and the locations of the thermocouples and HTF tubes within the HXs with different eccentricities. The eccentricity is defined in Eq. (1) for the proposed geometries [38,40].

$$\mathrm{ec} = \frac{L_d}{L_{max}} \tag{1}$$

where L_d indicates the distance between the centers of the shell and inner tube, and L_{max} represents the maximum value of L_d, as illustrated in Fig. 5.

2.3. Experimental procedure

In order to fill HXs with liquid PCM, solid paraffin was first heated at 80 °C until it melted. To avoid air pockets in the solid PCM, the melted PCM was carefully poured, layer by layer, into the enclosure. Before applying the next layer of liquid PCM, each layer of liquid PCM was allowed to completely solidify for approximately 30 min. This procedure was iterated until the container was filled with solid PCM. To ensure that the PCM was at a consistent temperature at the start of the experiments, the HX was exposed to a conditioned lab temperature of 25±2 °C for at least 24 h before initiating the experiment. To account for the variation in volume of solid PCM during the melting process, an empty space was provided at the end of the HX to store the additional melted PCM. The HXs were tested at HTF inlet temperatures of 85 °C. The Rayleigh and Stefan numbers, which are non-dimensional quantities, are determined for the charging temperatures using the following formulas [11]:

$$Ra = \frac{g\beta(T_w - T_m)D_h^3}{\nu\alpha} \tag{2}$$

$$Ste^* = \frac{C_{p,s}(T_m - T_0) + C_{p,l}(T_w - T_m)}{h_{sl}} \tag{3}$$

where D_h is hydraulic diameter calculated from Eq. (4).

$$D_h = \frac{4A_h}{P_h} \tag{4}$$

where A_h is the cross-sectional area of the confined PCM and P_h represents the wetted perimeter of the conduit, respectively. The Rayleigh and Stefan numbers corresponding to the charging temperature of 85 °C are 6.28×10^6 and 0.69, respectively. The PCM melting process started with circulating hot water using a centrifugal pump. This process went on until the entire PCM was completely melted. To visualize and document the progression of the solid-liquid interface during the melting process, photographs were taken every five minutes by lifting the front side insulation. During the experiment, the temperatures of the PCM at predefined locations were recorded every two seconds. A specialized lighting technique in photography was employed to facilitate the distinction between the solid and liquid PCM phases.

3. Data reduction

3.1. Liquid fraction

Digital photos were utilized to calculate the liquid fraction of PCM using the MATLAB Image Processing Toolbox. Before computing the melting fraction, the photos were filtered and adjusted for contrast to enhance quality. The processed images were then converted to grayscale and, subsequently, to a binary format. A two-dimensional matrix with elements of 0 and 1, representing black pixels (liquid PCM) and white pixels (solid PCM), respectively, was used to store the photos in binary format. The ratio of the number of pixels with a value of 0 (representing liquid PCM) to the total number of pixels in the image is calculated as the apparent liquid fraction (Eq. (5)).

$$\gamma_a = \frac{NP_0}{NP_t} \tag{5}$$

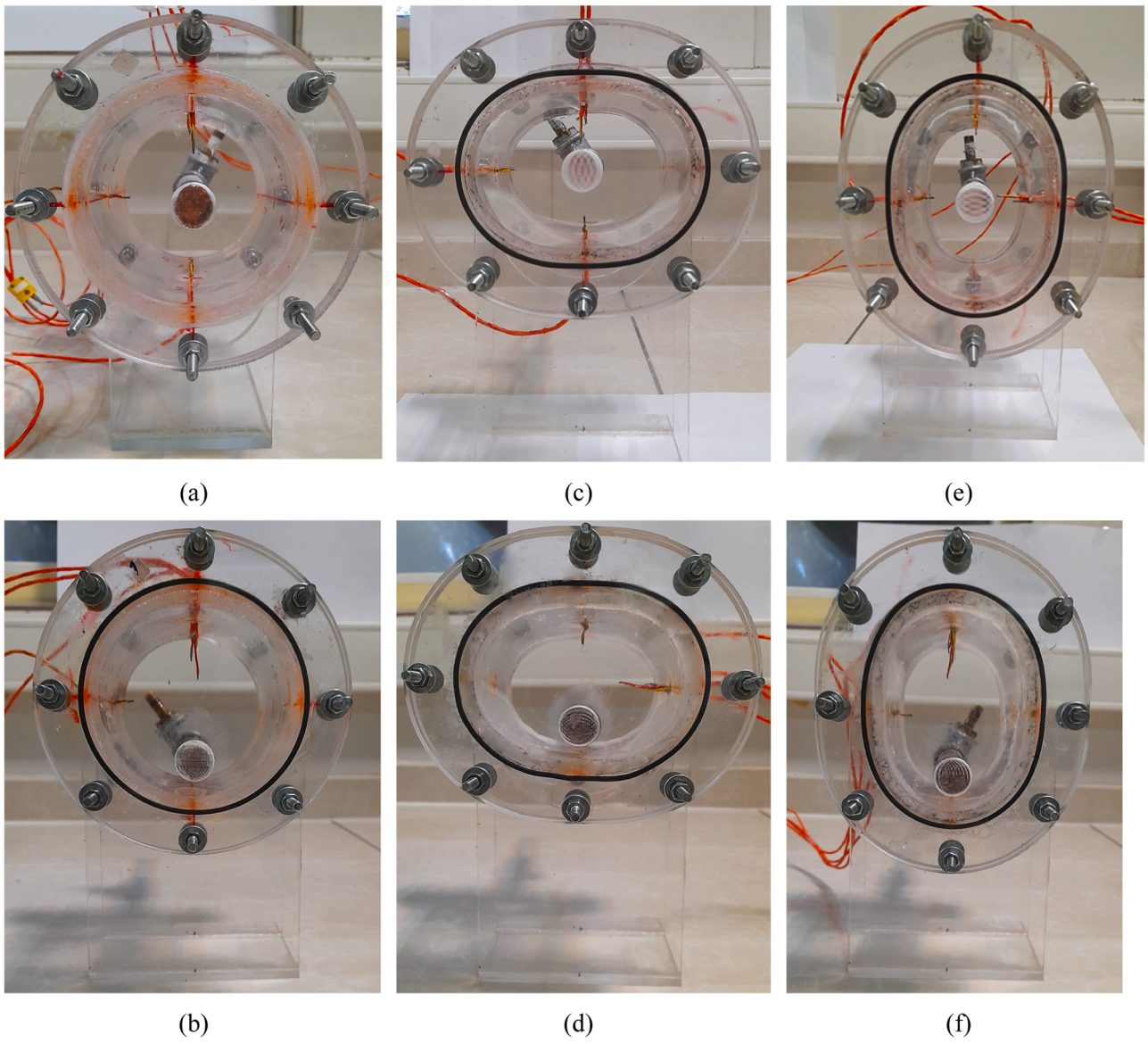

Fig. 2. Photographs of the different LHS units: (a) Circle (ec= 0), (b) Circle (ec= 0.8), (c) Horizontal obround (ec= 0), (d) Horizontal obround (ec= 0.8), (e) Vertical obround (ec= 0), (f) Vertical obround (ec= 0.8).

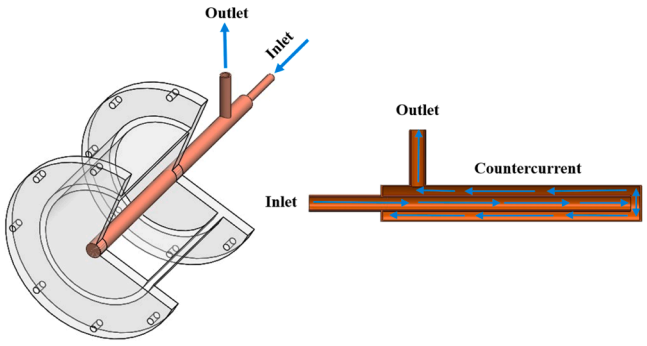

Fig. 3. Schematic drawing of the LHS heat exchanger.

NP_0, NP_t, and γ_a indicate the number of pixels with 0 values (liquid PCM), the total number of pixels, and the apparent liquid fraction, respectively. Due to the volume expansion of the PCM during melting, the liquid PCM filling the intentionally created gap at the end of the HX must be taken into account when calculating the actual liquid fraction. Thus, Eq. (5) is modified as follows [45].

$$\gamma_r = \frac{\gamma_a(1+\varnothing)}{1+\phi\gamma_a} \tag{6}$$

where γ_r and $\varnothing$ represent the real liquid fraction and volume change due to a phase change of PCM, respectively.

3.2. Heat transfer rate

The heat transfer rate from the inner tube to the PCM is computed from the thermal energy stored in the PCM in the form of sensible and latent heat during the melting process. Therefore, the total stored energy in PCM can be determined by utilizing Eq. (7):

$$Q_{total}(t) = \int_{V_l(t)} p_S c_s (T_{m1} - T_i) dV_l + \int_{V_l(t)} p_l c_l \left(T_{mean_l}(t) - T_{m2}\right) dV_l + \int_{V_s(t)} p_s c_s (T_{mean_s}(t) - T_i) dV_s + p_l \gamma_r(t) V_e (1 + \varnothing\gamma_a(t)) h_{sl} \tag{7}$$

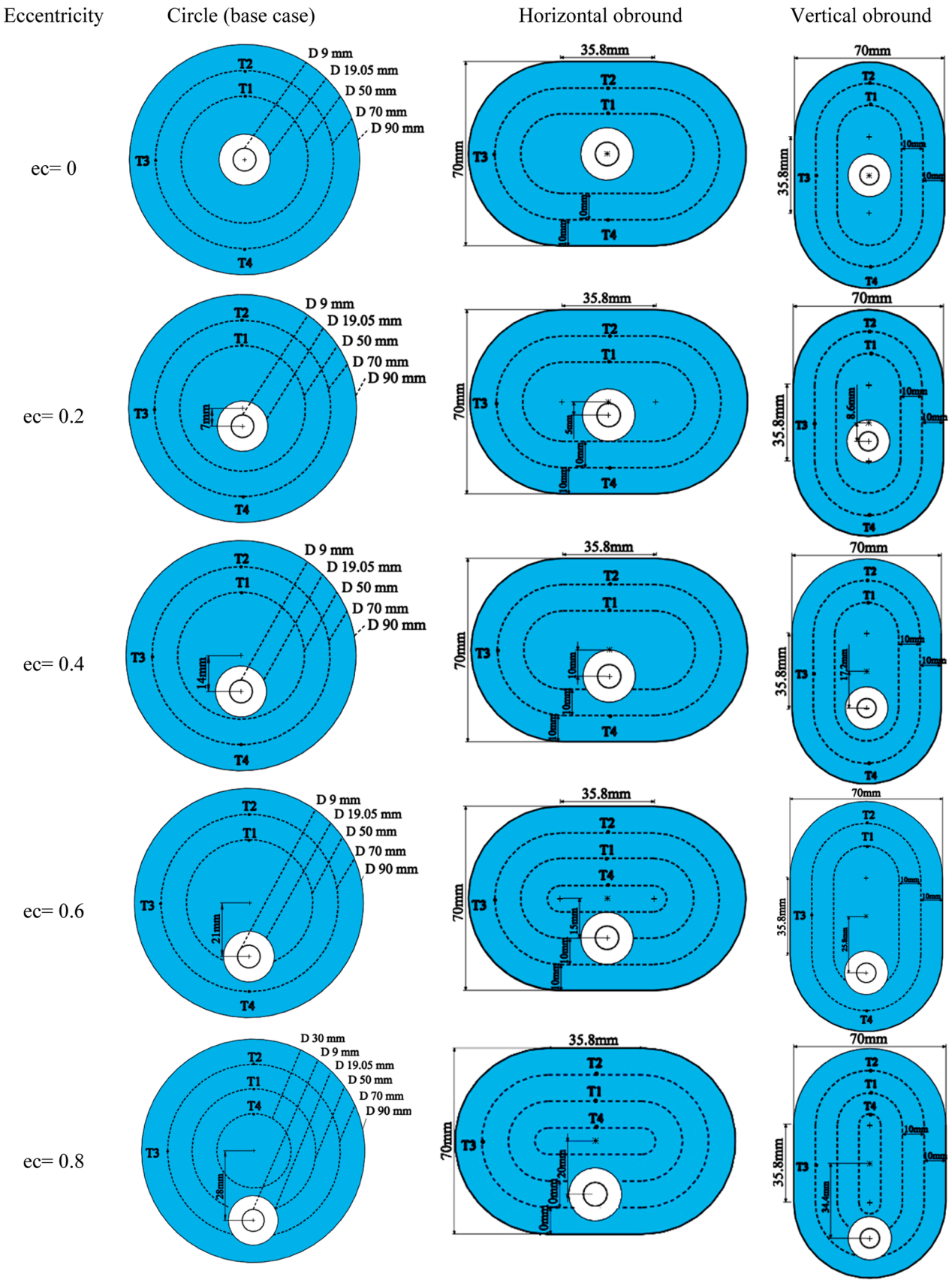

Fig. 4. Locations of thermocouples and HTF tubes in HXs with various eccentricities.

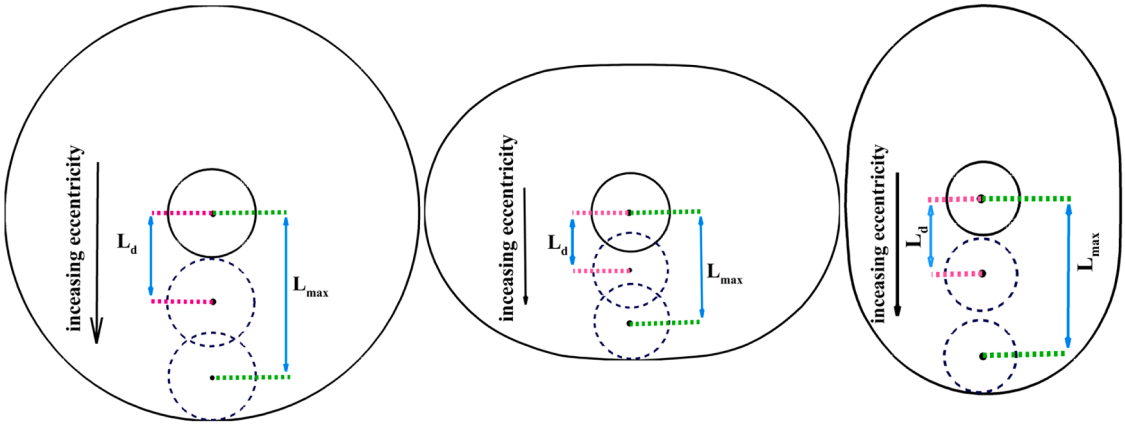

Fig. 5. Illustration of different shell geometries with L_d and L_{max}.

The average temperatures of the PCM in the liquid and solid phases at a certain time are denoted as $T_{mean_l}(t)$ and $T_{mean_s}(t)$, respectively. The first integral in Eq. (7) signifies the sensible heat absorbed by the PCM in the solid phase until it reaches its melting temperature. The second term refers to the superheating of the liquid PCM, while the third integral describes the absorption of sensible heat by the remaining solid PCM. Additionally, the latent heat is evaluated in the fourth term.

The following relation is used to calculate the heat transfer rate from the HTF tube to the PCM during the time period of Δt:

$$\dot{Q}(t) = \frac{Q(t+\Delta t) - Q(t)}{\Delta t} \tag{8}$$

During the total melting time, the time-averaged heat transfer rate is computed as Eq. (9):

$$\overline{\dot{Q}} = \frac{1}{t_{total}} \int_0^{t_{total}} \dot{Q}(t)\mathrm{d}t \tag{9}$$

where $\dot{Q}$ and t_{total} represent the averaged heat transfer rate from the inner tube to the PCM over Δt and the total melting time of the PCM, respectively.

The heat transfer rate from the HTF tube to the PCM can be expressed in terms of Nusselt numbers, as defined by Eq. (10).

$$Nu(t) = \frac{\dot{Q}(t) D_h}{A(T_w - T_m)k_l} \tag{10}$$

where $\dot{Q}(t)$, D_h, and A represent the instantaneous heat transfer rate, hydraulic diameter, and total heat transfer area, respectively. Meanwhile, k_l is the thermal conductivity of the liquid PCM.

The time-averaged Nusselt number is calculated for different HXs using Eq. (11).

$$\overline{Nu} = \frac{1}{t_{total}} \int_0^{t_{total}} Nu(t)d(t) \tag{11}$$

4. Experimental results

The purpose of this study is to examine how the eccentricity of the HTF tube in the three different shell geometries affects the behavior of the melting front, temperature history, liquid fraction, Nusselt number, total melting time, time-averaged heat transfer rate, and time-averaged Nusselt number. To achieve this goal, fifteen various types of HXs have been developed.

4.1. Experimental reproducibility

To ensure experimental repeatability, the melting process was repeated twice in the circular, horizontal, and vertical obround shells with eccentricity values of 0.6, 0.4, and 0.8, respectively. The transient liquid fractions obtained from two different trials are depicted in Fig. 6. The findings show that the transient liquid fraction demonstrates a repeatable pattern with minor variations. To quantify these variations, the root mean square error (RMSE) between two data sets was determined as indicated in Eq. (12).

$$RMSE = \sqrt{\frac{1}{N}\sum_{n=1}^{N}\left(\gamma_{exp1,n} - \gamma_{exp2,n}\right)^2} \tag{12}$$

where N and γ indicate the number of data and liquid fraction, respectively. The RMSE for liquid fraction in HXs with circular, horizontal, and vertical obround shells were 1.1 %, 0.9 %, and 1.9 %, respectively.

4.2. Melting performance analysis

4.2.1. Visualization of the melting front

Visualizing the development of the melt front reveals important information about the behavior of PCM and the primary mode of heat transfer during the melting process. Observing and comparing melting processes in various HXs helps to understand melting phenomena and how variables such as HTF tube eccentricity in different shell geometries affect the melting rate. Fig. 7 illustrates the evolution of the melting front in LHS units with a circular shell at various eccentricity factors through experimental observations. In these photographs, the white and black areas represent the solid and liquid phases, respectively. The use of specialized lighting in the photography makes the solid-liquid interface visible. In the early stages of the melting process (Fig. 7(a_0-e_0)), the photographs indicate the formation of a thin layer of melted PCM surrounding the hot surface of the inner tube, which appears to be the same for all concentric and eccentric HXs, with no apparent superiority between these configurations, suggesting similar melting rates and conduction as the predominant heat transfer mechanism. Conduction continues to be the dominant heat transfer mechanism as long as the viscous forces are strong enough to inhibit fluid movement, resulting in the circular expansion of the melting area. By developing the melting area, the buoyancy force overcomes the viscous force, causing the natural convection current to begin and becoming the predominant melting mechanism. During this stage, the hot, liquid PCM ascends and the cold, liquid PCM descends due to the density difference between them, creating liquid circulations and enhancing the melting process, as evidenced by the formation of an oval-shaped interface (Fig. 7(a-e) $_{(1)}$). As melting progresses, the natural convection current, the predominant

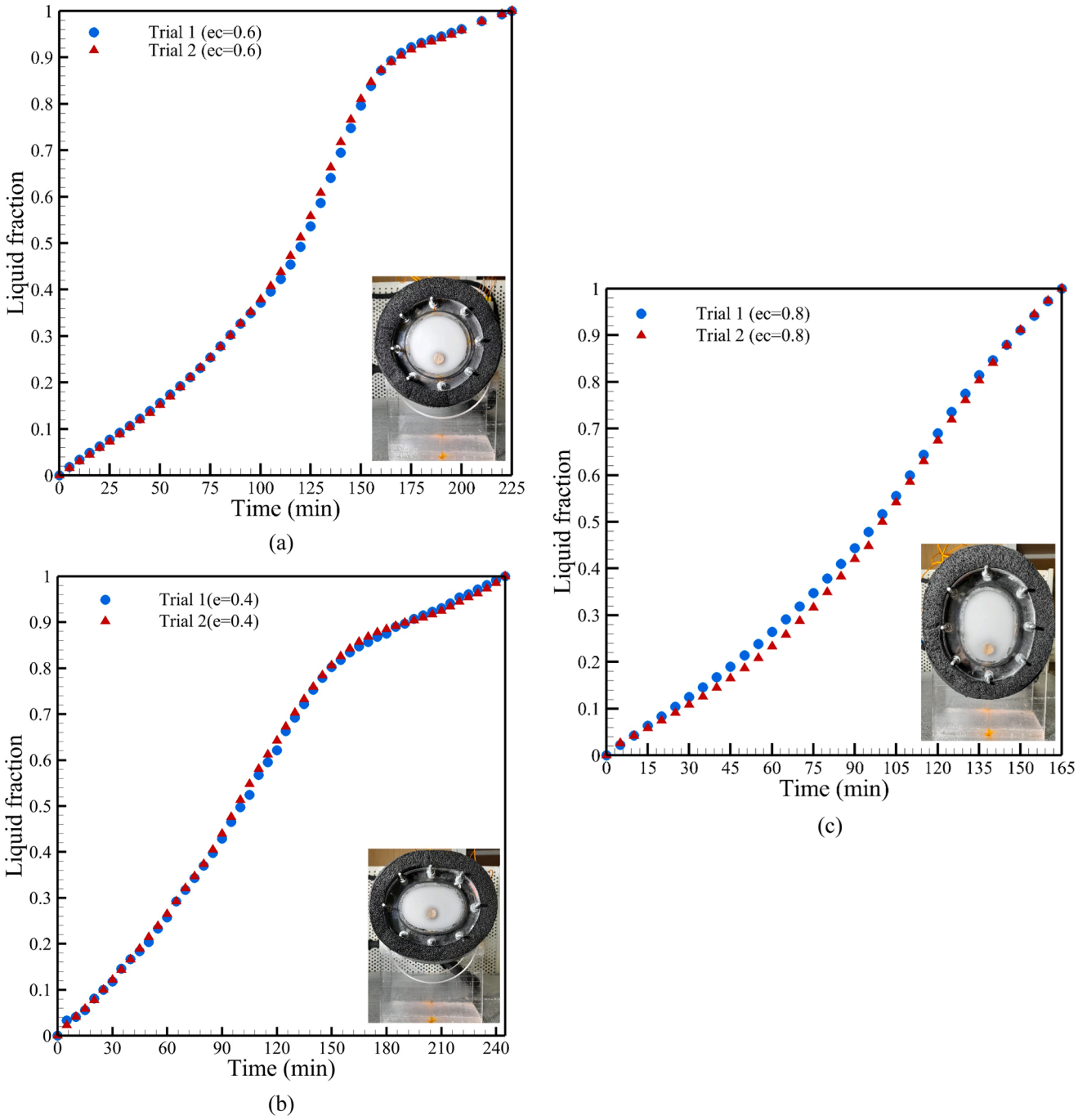

Fig. 6. Repeatability of transient liquid fraction: (a) Circular shell (ec= 0.6), (b) Horizontal obround shell (ec= 0.4), (c) Vertical obround shell (ec= 0.8).

melting mechanism, becomes stronger and has a more noticeable effect on the melting front progression. This impact is evidenced by the increased surface area of the melting front in the upper part of the enclosure (Fig. 7(a-e) $_{(2–4)}$). As demonstrated in Figs. 7(a_4) and Fig. 7(b-d) $_{(5)}$, the solid PCM above the HTF tube melts entirely, but only a limited amount of solid PCM below the HTF tube melts due to the low heat transfer rate by conduction. A comparison between Fig. 7(a_4) and Fig. 7(a_5) clearly indicates that the solid-liquid interface moves downward at a slower rate below the inner tube compared to the top part. This observation supports our previous statement that in the lower part of the HX, melting is mainly governed by conduction, resulting in partial melting of the PCM, which can greatly increase the total melting time. The eccentricity of the HTF tube has a significant impact on increasing the rate of the melting process and thereby reducing the complete melting time. This can be explained by the fact that in the HX with the eccentric configuration, a greater amount of PCM is accommodated in the upper part of the inner tube, benefiting from the existence of convection flows (Fig. 7(b-e) $_{(1–4)}$). Additionally, the eccentric tube configuration exposes a smaller amount of PCM below the HTF tube, where slower heat conduction is the dominant heat transfer mechanism (Fig. 7(b-e) $_{(5)}$). In other words, the downward movement of the HTF tube increases the melting rate in both the top and bottom regions of the HX simultaneously. As it is seen in Fig. 7, complete melting is achieved after 165 min from the start of the experiment in the HX with an eccentricity of 0.8, while solid PCM can still be observed in other HXs with smaller eccentricity values. In fact, at higher eccentricity factors (0.8), the optimal utilization of both conduction and convection heat transfer mechanisms has been employed to increase the rate of the melting

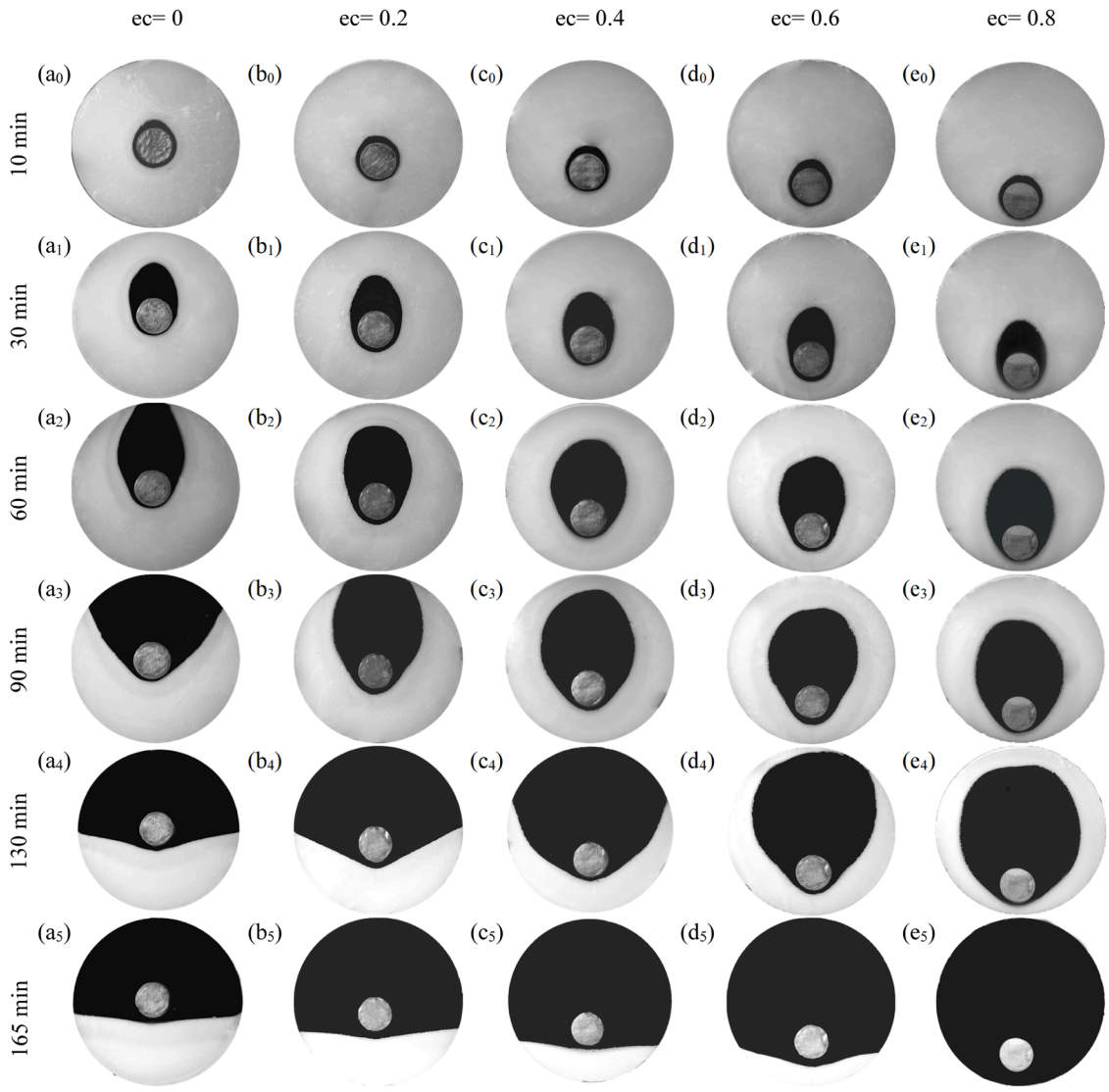

Fig. 7. Melt front evolution in LHS units with circular shell at various eccentricities.

process.

To better understand how the melting of PCM in the LHS units with various shell geometries is affected by inner tube eccentricity, the time variation of the melting front for the horizontal obround shell with different eccentricity factors is presented in Fig. 8. At the initial stages, the melting interface in both concentric and eccentric HXs is almost the same, like the circular shell, suggesting similar melting rates (Fig. 8(a-e) $_{(0)}$). As time progresses, the increased surface area of the oval-shaped melting front in the top part of the enclosure indicates that the melting rate has increased significantly at the upper part of the HTF tube compared to the lower part, due to natural convection being the predominant mechanism (Fig. 8(a-e) $_{(1–4)}$). In eccentric arrangements, contact between the melting interface and the upper adiabatic wall of the shell occurs at a later time compared to the concentric configurations. By increasing the eccentricity, the dominant convection area above the HTF tube expands, resulting in a larger amount of PCM exposed to the stronger natural convection current in the upper region. As a result, the rate of the melting process is enhanced more than in concentric configurations (Fig. 8(b-e) $_{(1–4)}$). Subsequently, as the solid-liquid interface begins to propagate downward, the melting process is primarily governed by a slow heat conduction mechanism. In the eccentric cases, less PCM is exposed to the sluggish conduction mechanism below the HTF tube, leading to a reduction in the total melting time (Fig. 8(b-e) $_{(5)}$). It is important to note that in the final stages of the melting process, the horizontal obround shell shows a faster melting rate compared to the circular shell because of providing a larger solid-liquid interface area during the thermal conduction domination stage.

Fig. 9(a-e) (0–5) illustrates the temporal variation in the melting process of the vertical obround shell at different eccentricities. As observed from the melting front in Fig. 9, it is evident that as the eccentricity factor increases from ec= 0 to ec= 0.8, the melting rate accelerates. Specifically, HX with an eccentricity factor of 0.8 achieves complete melting after 165 min, whereas solid PCM persists in the other HXs with smaller eccentricity factors. Upon further analysis of Fig. 9(e) $_{(0–5)}$, it becomes apparent that the melting process trend for the vertical obround shell with an eccentricity value of 0.8 varies from that of circular and horizontal obround shells. After 130 min, the PCM at the bottom of the shell has entirely melted, while the unmelted PCM remains at the top of the shell (Fig. 9(e) $_{(4)}$). The melting behavior observed is attributed to the shell geometry, particularly evident in the vertical obround shape, which accommodates a lesser volume of PCM below the HTF tube at an eccentricity of 0.8.

Fig. 10 shows the solid-liquid interface at various times in three different shell shapes with eccentricity values of 0, 0.4, and 0.8. The melting time can be expressed in terms of the non-dimensional Fourier number as follows [40]:

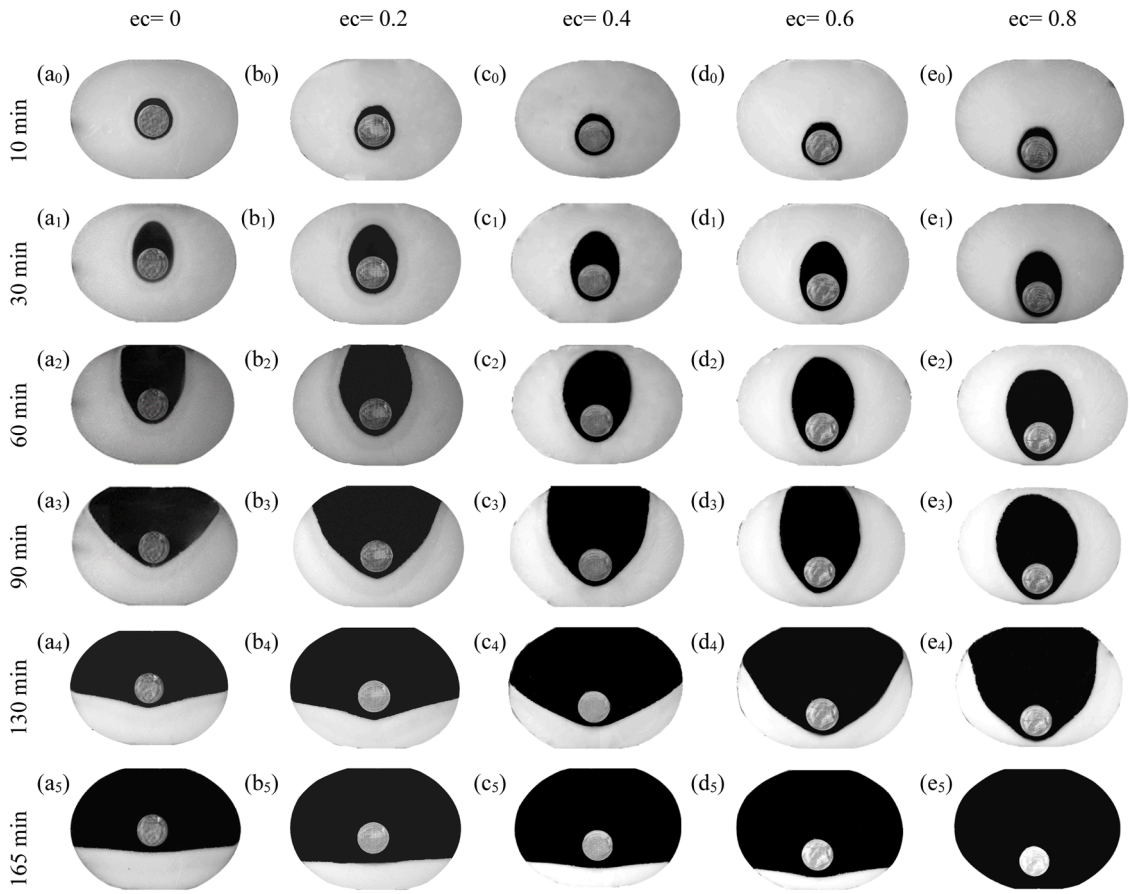

Fig. 8. Melt front evolution in LHS units with horizontal obround shell at various eccentricities.

$$Fo = \frac{\alpha t}{D_h^2} \tag{13}$$

where α and D_h represent the thermal diffusion coefficient and the hydraulic diameter, respectively. The Fourier numbers corresponding to the charging times in Fig. 10 are outlined in Table 3. Image processing was utilized to analyze the melting photographs and assess the advancement of the melt interface. This figure enables the observation and monitoring of melt interface movement in the studied HXs. Notably, an increase in the eccentricity factor results in the expansion of the solid-liquid interface area in the upper part of the HTF tube, indicating that a larger amount of PCM benefits from faster convection-dominated melting, while a smaller quantity of PCM is exposed to the slower heat conduction mechanism below the inner tube.

4.2.2. Temperature history

The record of the transient temperature history provided by the thermocouples offers important insights into the thermal behavior of the paraffin during the melting process. To assess the impact of HTF tube eccentricity on temperature profiles, Figs. 11, 12, and 13 depict the variation of recorded temperatures and the dimensionless temperature against time (in minutes) and Fourier number at predefined locations (T1-T4) for the examined LHS units. These temperature profiles were recorded at a tube wall temperature of 85 °C, corresponding to a Rayleigh number of 6.28×10^6 and a modified Stefan number of 0.69. The dimensionless temperature is defined as [46]:

$$\theta = \frac{T - T_m}{T_w - T_m} \tag{14}$$

where T_m and T_w represent the melting temperature of the PCM and the tube wall temperature, respectively. It can be observed that the recorded temperatures in different shell geometries exhibit similar trends, which can be attributed to the mechanisms of heat transfer during their respective phase change processes. Initially, the temperature of the thermocouples in all LHS units rises due to the heat conduction mechanism until reaching the melting temperature. During this stage, the rate of temperature increase in the upper part of the HXs is significantly higher. This indicates that the rate of heat transfer to the solid PCM has increased in the upper part of the annulus due to the formation of circulating convection currents in the liquid PCM, which move the heated liquid PCM upwards. Yazıcı et al. [35] and Avci et al. [47], who investigated the melting of paraffin in a horizontal tube-in-shell storage unit, observed similar temporal variation in temperature. As depicted in Figs. 11-13(a-b), an increase in the eccentricity factor leads to a delayed temperature increase in T1 and T2. This delay can be attributed to the longer distance between the thermocouples T1 and T2 and the HTF tube. Similar temperature behaviors were reported by Safari et al. [18] and Yazıcı et al. [35], with thermocouples located in the upper half region of HXs with concentric and eccentric tubes. The heat transfer mechanism continues through conduction until the temperatures remain below the melting point. After this step, the melted PCM flows over the tips of the thermocouples, leading to a further increase in temperature. By considering the temperature history inside the HX with eccentric tube, as the eccentricity factors increase, the improvement in the temperature of T1 and T2 declines due to the longer distance from the HTF tube, so the greatest improvement is observed in concentric cases. During this stage, the thermocouples in the upper part of the HTF tube, T1 and T2, record some fluctuations. These fluctuations are induced by differences in the density of the melted PCM, leading to the formation of chaotic flow structures and vortices within the liquid PCM [14]. The presence of these fluctuations in the upper part of the enclosure was also reported in the literature [18]. Afterward, the liquid PCM gains sensible heat, and its

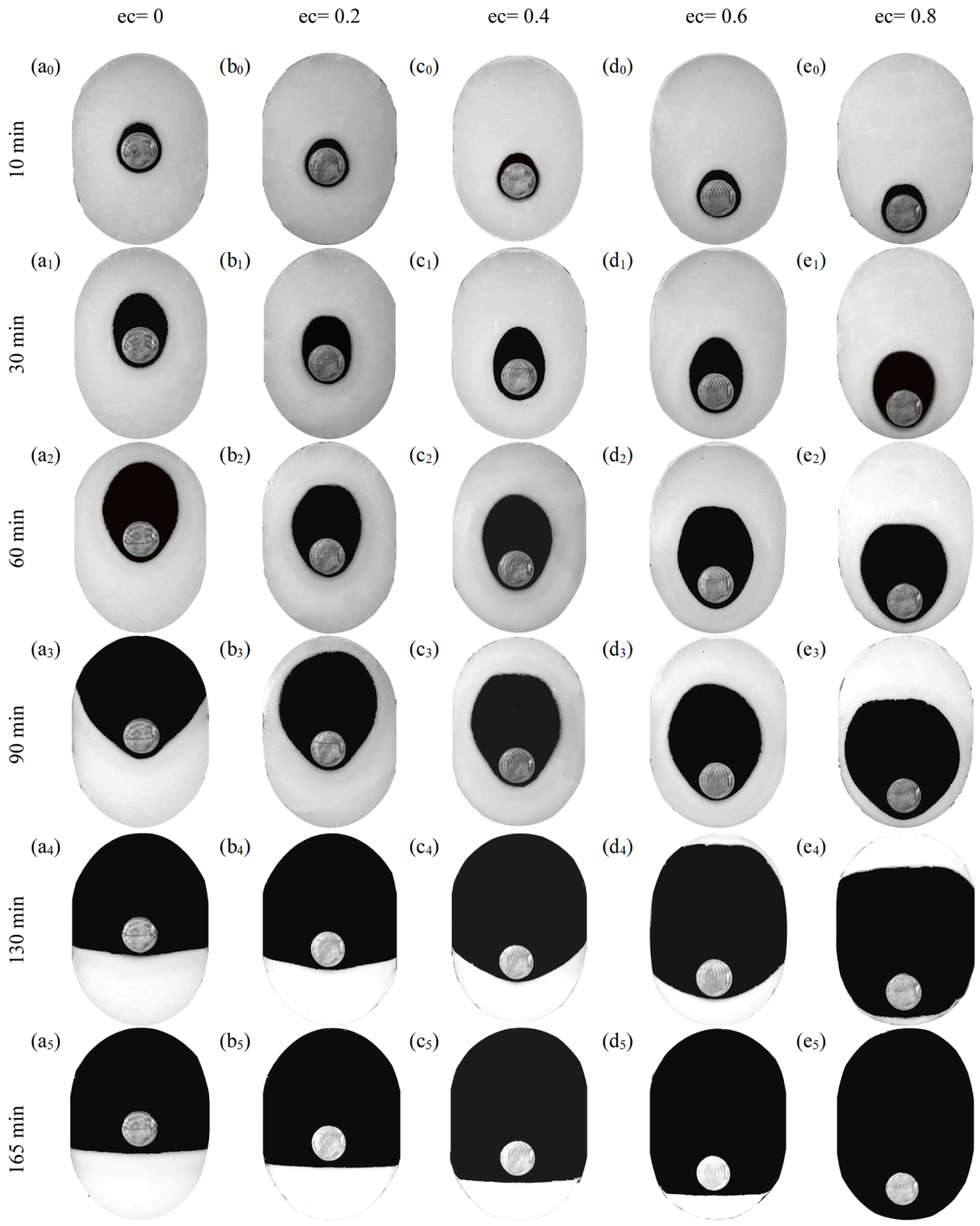

Fig. 9. Melt front evolution in LHS units with vertical obround shell at various eccentricities.

temperature gradually approaches the HTF tube temperature (Figs. 11-13(a-b)). The thermal behavior of the thermocouple in the lower part of the HTF tube, T4, differs significantly from that of the thermocouples located in the upper part. The nearly linear increase in temperature of T4, without any fluctuations, implies that heat conduction significantly influences the lower section of the HXs, resulting in a slower rate of melting in that region. As depicted in Figs. 11-13(d), an increase in the eccentricity factors leads to improved melting in the lower part of the HTF tube, resulting in a higher temperature at the T4 thermocouple. This enhancement can be attributed to the shorter distance between the HTF tube and the T4 thermocouple, leading to an increase in heat conduction. This temperature behavior was also reported in [35,47], for thermocouples located in the lower part of the HTF tube in both concentric and eccentric configurations. As shown in Fig. 4, due to the limited space at the lower part of the HTF tube at an eccentricity of 0.8 for the three shell shapes and 0.6 for the horizontal obround shell, the position of the T4 thermocouple has been modified. In these cases, the T4 thermocouple is located at the upper part of the HTF tube. Consequently, the temperature behavior of the T4 thermocouple in these cases is similar to that of thermocouples positioned at the upper part of the HTF tube (Figs. 11-13(d)). Based on Figs. 11-13, it is evident that the thermocouples positioned in the upper part of the HTF tube (T_1, T_2, and T_3) exhibit higher temperatures compared to those positioned in the lower part (T_4). The behavior validates the presence of a rotating

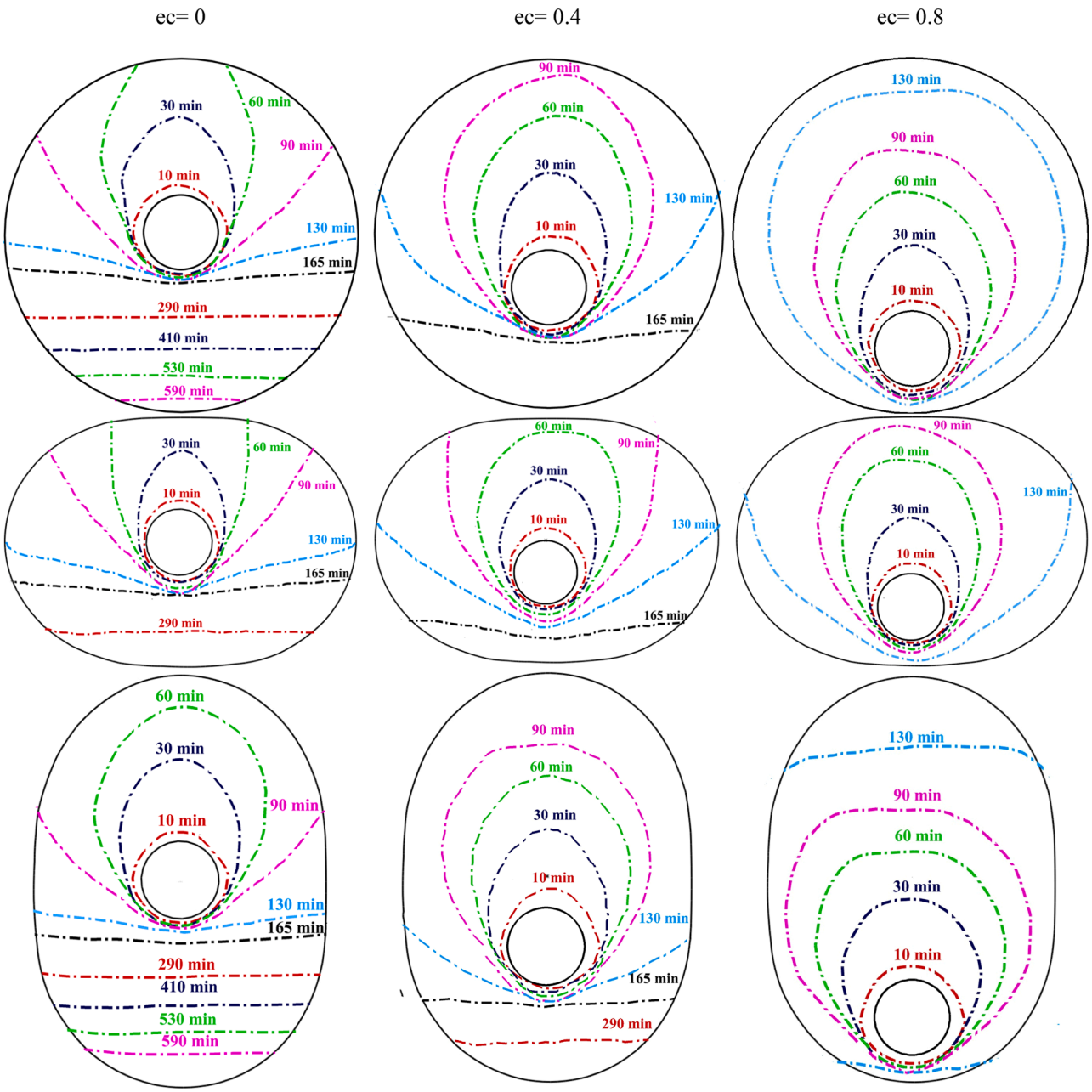

Fig. 10. Progression of solid-liquid interface in LHS units with various eccentricities and shell geometries.

Table 3
Fourier numbers corresponding to times (min).

Time (min)	10	30	60	90	130	165	290	410	530	590
Fourier number	0.01	0.03	0.07	0.11	0.16	0.21	0.37	0.53	0.68	0.76

current in the melted PCM at the upper section.

4.2.3. *Melt fraction*

The variation of liquid fractions with time (in minutes) and Fourier number at different eccentricity factors for the three LHS units is shown in Fig. 14. It can be observed that, for $t \leq 10$ min (Fo ≤ 0.013), the liquid fraction curves for all LHS units with eccentric and concentric HTF tubes coincide and exhibit a linear trend with a high slope. This steep slope implies a fast-melting rate due to the large temperature difference over a small layer of molten PCM surrounding the HTF tube, where thermal conduction resistance is minimal. As the melting progresses, the liquid fractions gradually transition from a nearly linear trend to a curved one with a decreasing slope. This transition occurs when the solid PCM in the upper part of the HTF tube is completely liquefied. During this time, natural convection weakens, and heat conduction becomes the predominant mechanism. It can be observed that an augmentation in the eccentricity factor leads to a delay in the transition from a linear to a curved pattern. This phenomenon can be explained by the fact that increasing the eccentricity exposes a larger portion of the annular region to the natural convection current, resulting in a delay in this transition as

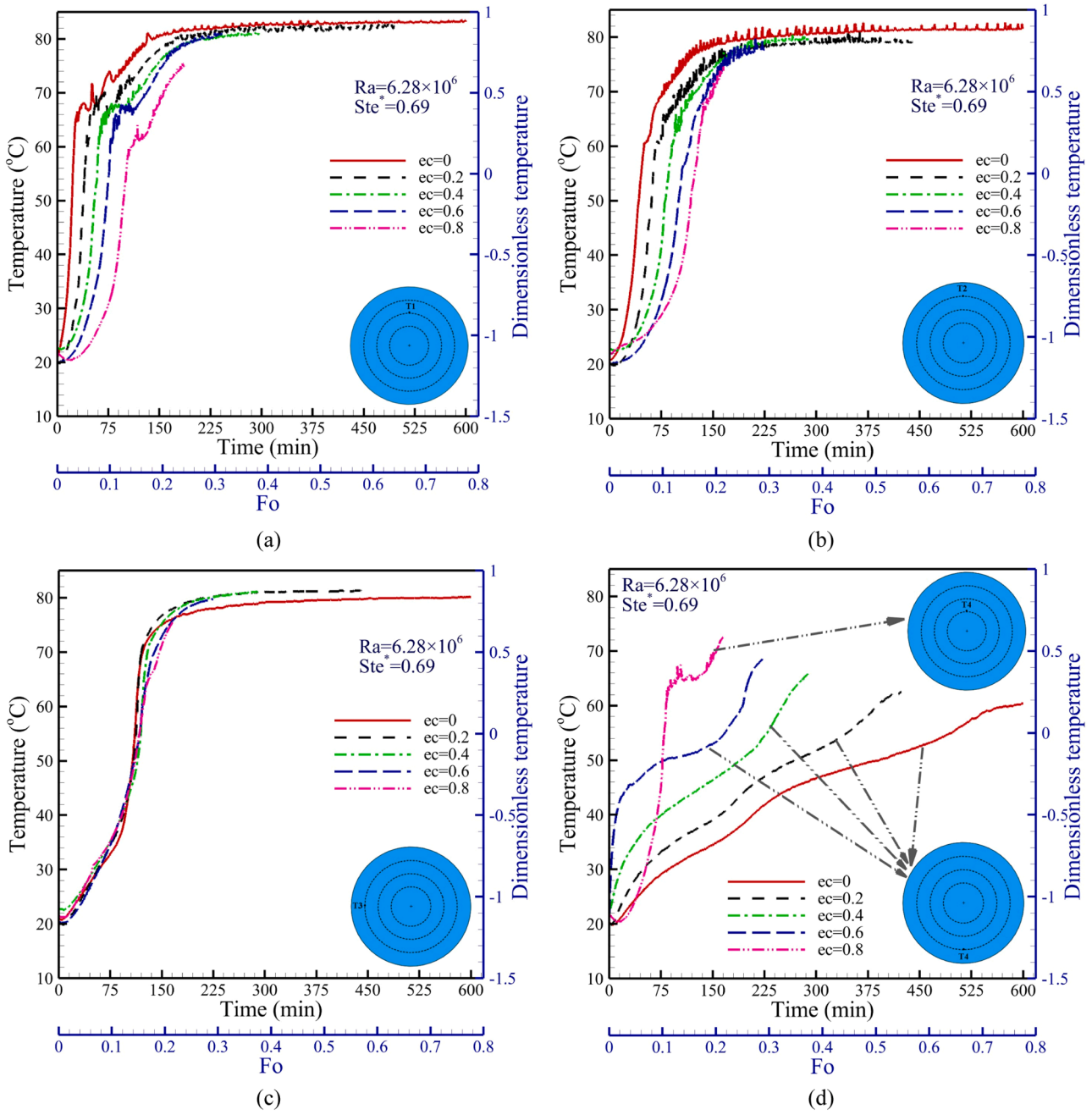

Fig. 11. Temperature history of the thermocouples for LHS units with circular shell at various eccentricities.

it takes more time to melt the PCM in the upper part of the inner tube. In all shell geometries with an eccentricity factor of 0.8, the liquid fractions maintain a consistent linear trend during the entire melting process. This behavior can be attributed to the continuous dominance of natural convection throughout the process. However, in HXs with eccentricity factors ranging from 0 to 0.8, the time period during which the liquid fraction exhibits a curvilinear trend increases as the eccentricity factor decreases. This thermal behavior can be explained by the fact that the volume of the PCM below the HTF tube increases as the eccentricity factor decreases. Consequently, a significant portion of the solid PCM beneath the HTF tube melts after the PCM in the upper part of the enclosure has fully melted. At this stage, natural convection strength diminishes, and melting is predominantly governed by slow conduction heat transfer. A similar trend for liquid fraction during melting in circular shells with eccentric tubes has been reported by Pahamli et al. [37] and Darzi et al. [48].

4.2.4. *Melting time*

In order to thoroughly analyze the melting process in the three shell configurations with various eccentricity factors, this section compares the complete melting time and the variation of melting time reduction for all cases. Fig. 15 illustrates the influence of HTF tube eccentricity on the complete melting time (in minutes) and the dimensionless total melting time (Fo_{tot}) in different shell geometries. As depicted in Figs. 15, while comparing the concentric HXs, it is observed that modifying the shell geometry from a circle to a horizontally oriented obround shape significantly reduces the total melting time from 600 min (Fo = 0.77) to 410 min (Fo= 0.53), representing a reduction of 32 %. In contrast, the vertically oriented obround shell reduces the melting rate, resulting in a longer complete melting time of 680 min (Fo = 0.87), which extends the total melting time by 13 %. Notably, the HXs with circular, horizontal, and vertical obround shells at an eccentricity factor of 0.8 exhibited significant reductions in total melting time in comparison to their

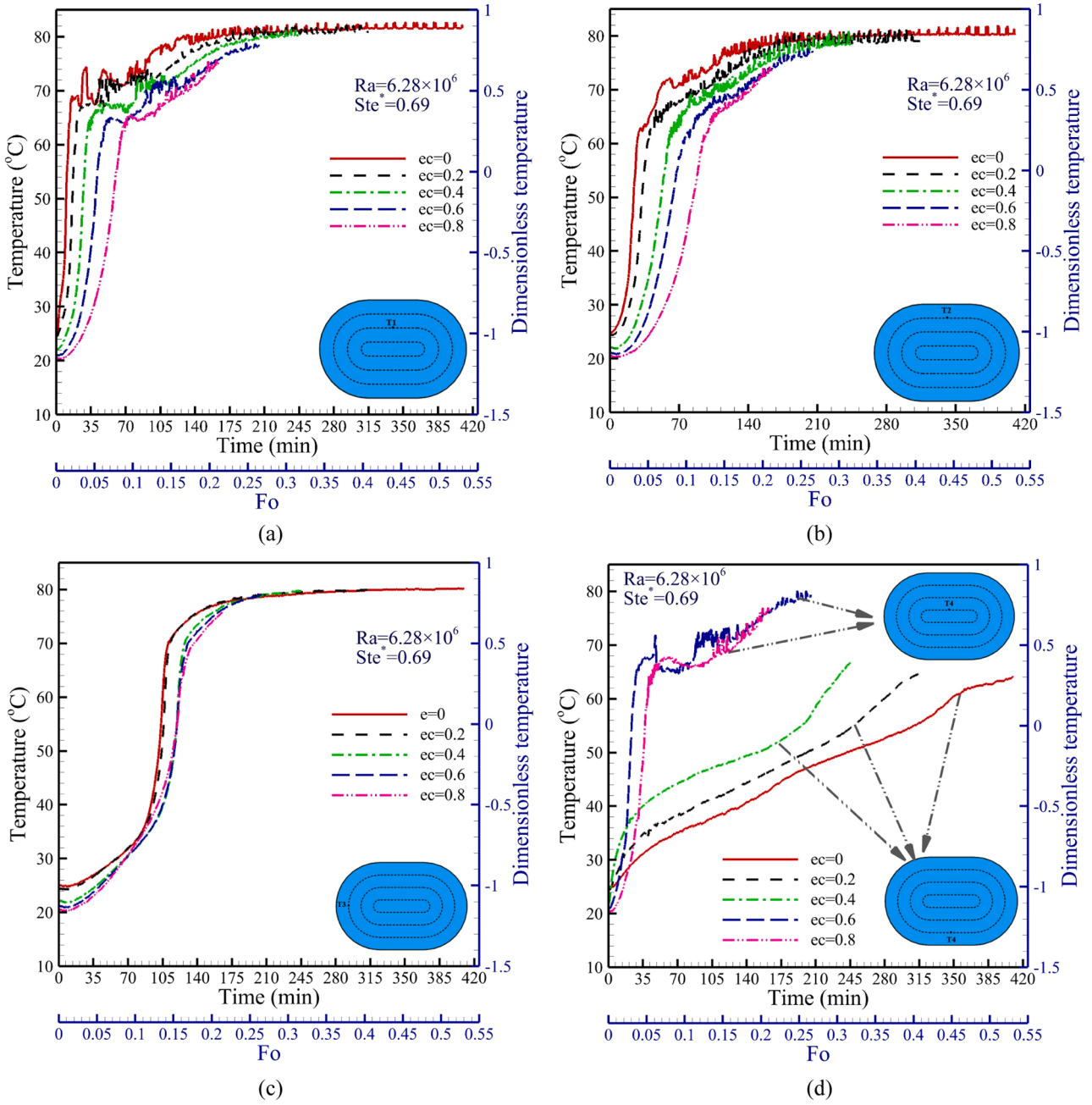

Fig. 12. Temperature history of the thermocouples for LHS units with horizontal obround shell at various eccentricities.

corresponding concentric tube HXs, with reductions of 72 %, 60 %, and 76 %, respectively. Zheng et al. [40] similarly reported a 73 % reduction in the total melting time during the melting process of n-octadecane in a circular double pipe HX with an eccentricity factor of 0.8 at a Rayleigh number of 1.21×10^7. The discrepancy between the present results and existing literature can be attributed to differences in Rayleigh number, PCM types, and tube dimensions. In addition, Harmen et al. [49], who investigated the melting of paraffin in horizontal double-pipe HXs, reported a 54 % reduction in melting time at an eccentricity factor of 0.5. Moreover, Fig. 15 clearly demonstrates that as the eccentricity factor increases from 0 to 0.8, the difference in melting time among the studied geometries diminishes. It can be inferred that, despite the decrease in melting time with an increase in the eccentricity factor, the optimal shell geometry should be selected for each eccentricity factor to attain optimal thermal performance.

The relationship between the eccentricity factor and melting time reduction for the studied cases is depicted in Fig. 16. Melting time reduction quantifies the decrease in melting time relative to the concentric circular shell, which is considered the base case. At constant HTF tube eccentricities of 0.2, 0.4, and 0.6, the horizontal obround shell exhibits the shortest total melting time, with corresponding melting time reductions of 47 %, 59 %, and 66 %, respectively. However, for the same eccentricity factors, the vertical obround shell shows the smallest melting time reductions of 18 %, 47 %, and 61 %, respectively. The maximum melting time reduction of 72 % is observed at the largest eccentricity (ec = 0.8) for all geometries.

4.2.5. *Heat transfer characteristics*

The variation of the Nusselt number as a function of the dimensionless time (Fo) for the studied cases is shown in Fig. 17. The Nusselt number variations reflect the presence of different heat transfer mechanisms during the melting process. Based on the variation in the Nusselt

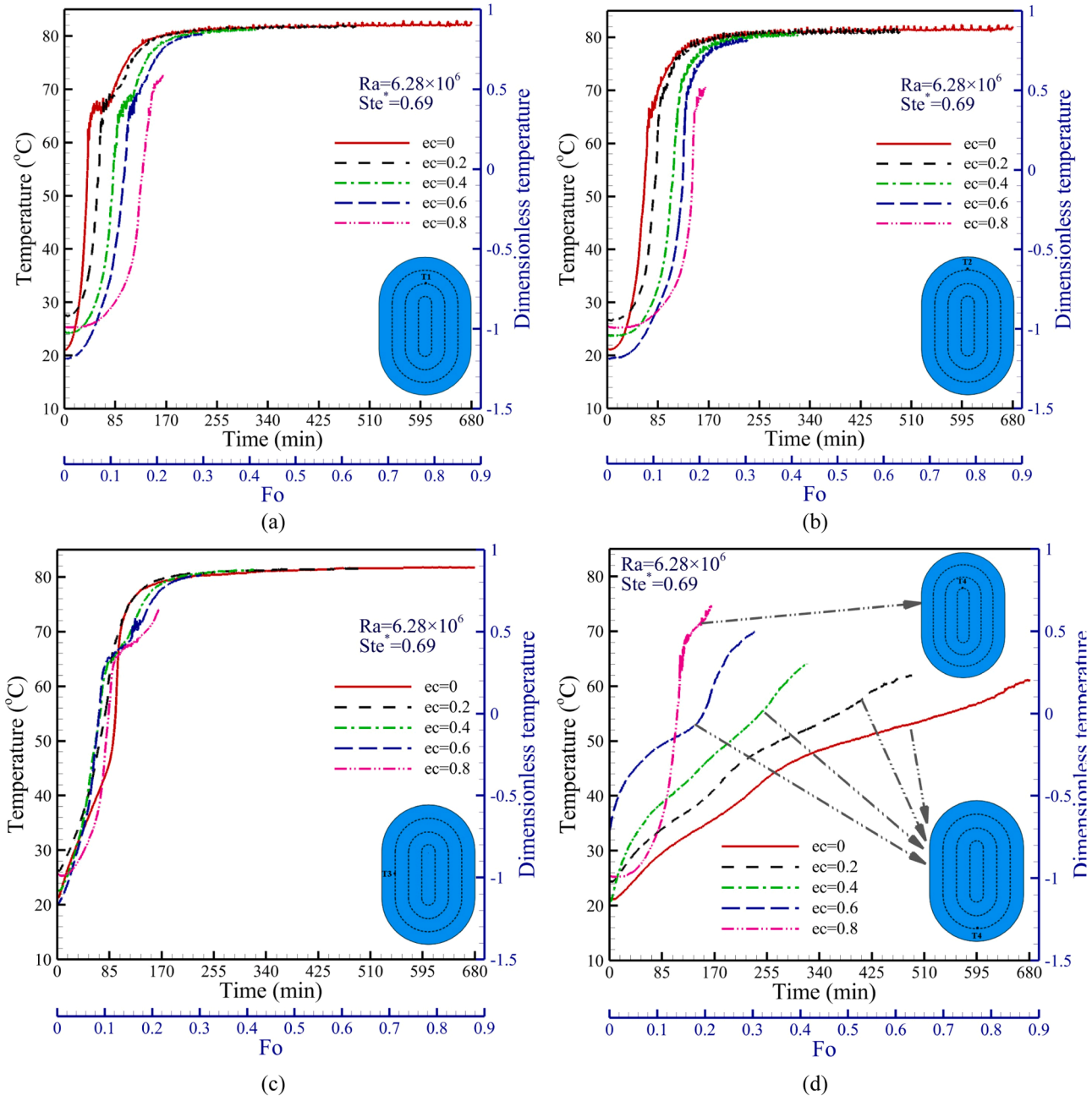

Fig. 13. Temperature history of the thermocouples for LHS units with vertical obround shell at various eccentricities.

number, the melting process can be divided into three distinct melting stages, namely: conduction dominance, convection dominance, and convection diminishing [11]. In all cases, in the early stages of the melting process, close-contact melting heat transfer occurs between the HTF tube surface and the formation of a thin layer of liquid surrounding the HTF tube. This leads to a significant rate of conduction heat transfer, resulting in an initial high Nusselt number for all eccentricities (conduction-dominated). However, as the thickness of the liquid layer increases, the thermal resistance between the HTF tube and the solid-liquid interface increases, causing a sharp reduction in the Nusselt numbers. As previously mentioned, as the melting area develops, the primary mode of heat transfer transitions to natural convection. Consequently, the decline in the Nusselt number ceases, leading to a gradual improvement in the heat transfer rate. Indeed, in the balance between a decreasing heat transfer rate caused by thermal resistance and an increasing heat transfer rate due to natural convection current, the latter prevails, resulting in a rise in the Nusselt number. Additionally, as the eccentricity increases, the dominant convection area above the HTF tube expands, resulting in stronger and more persistent natural convection heat transfer. Consequently, the trend of increasing the Nusselt number is further enhanced with increasing eccentricity due to the emergence of a more robust natural convection current (convection-dominated). As time passes, the solid PCM in the upper part of the HTF tube is completely liquefied, and the melting interface progresses under the HTF tube, where convection current is weakened and melting is mainly governed by conduction; as a consequence, the Nusselt number begins to decrease (diminishing convection). For HXs with different eccentricity factors, the points at which the diminishing trend begins align with the times when the rate of liquid fraction increase starts to decrease. As depicted in the figure, an increase in the eccentricity factor can effectively prolong the convection-dominated melting and postpone the diminishing convection to the very end of the melting

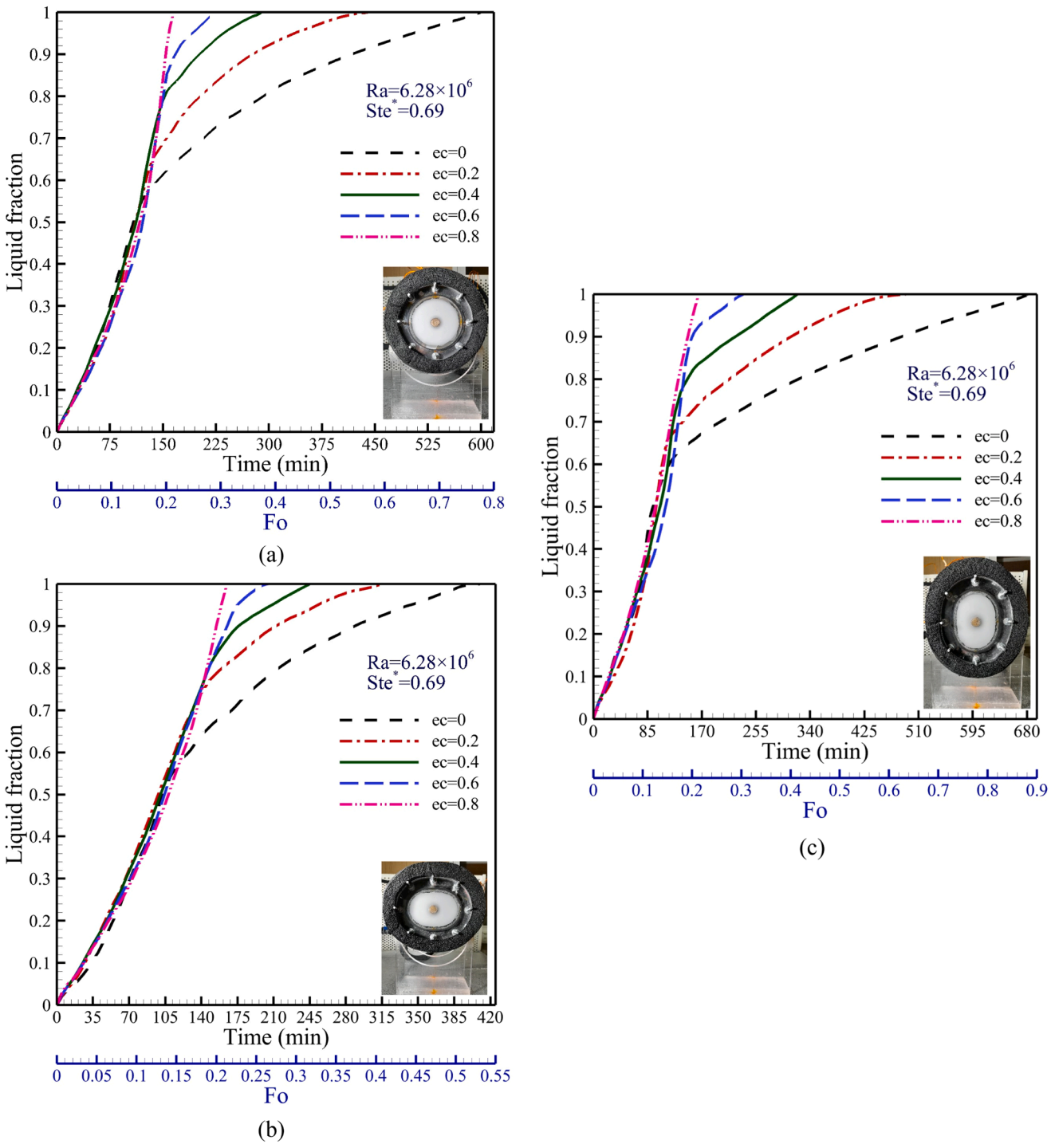

Fig. 14. Transient liquid fraction in LHS units with various eccentricities: (a) Circular shell, (b) Horizontal obround shell, (c) Vertical obround shell.

process. The variation of the heat transfer coefficient under different eccentricity values has been similarly reported by Cao et al. [50] through the melting process in an eccentric horizontal shell and tube storage unit.

The variation of the time-averaged heat transfer rate and Nusselt number with eccentricity factor are depicted in Fig. 18. It is observed that for all shell geometries, the time-averaged heat transfer rate and Nusselt number increase with increasing eccentricity due to the formation of a larger convection-dominated heat transfer area in eccentric configurations, which accordingly increases the heat transfer rate. The maximum time-averaged heat transfer rate and Nusselt number are achieved at an eccentricity of 0.8. In comparison to the corresponding concentric cases, the circular, horizontal, and vertical obround shells at an eccentricity of 0.8 demonstrate a significant improvement of 246 %, 151 %, and 304 %, respectively. These findings indicate that by increasing the eccentricity, the vertical obround shell contributes more effectively to heat transfer enhancement compared to the other two HXs. Moreover, as shown in Fig. 18, it is observed that at constant eccentricity factors of 0, 0.2, 0.4, and 0.6, the highest time-averaged heat transfer rates are achieved with the horizontal obround shell, with improvements of 38 %, 29 %, 10 %, and 4 %, respectively, as compared to the circular enclosure. Conversely, the time-averaged heat transfer rates for

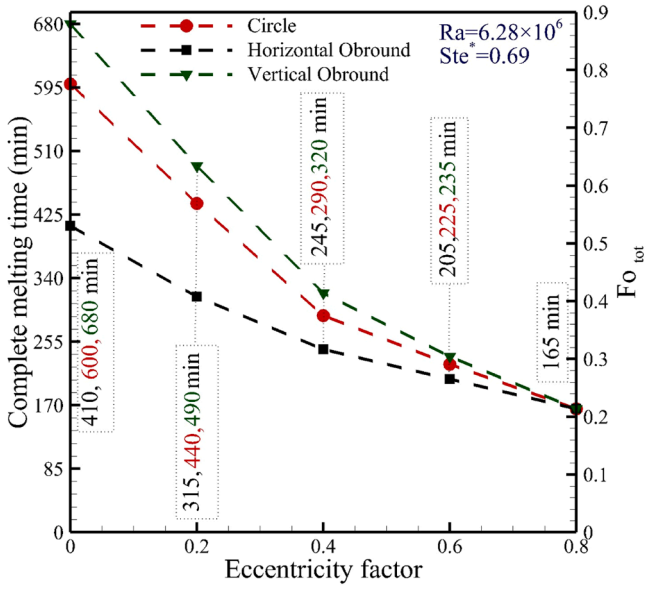

Fig. 15. Comparison of complete melting time (min) and Fo_{tot} for different shell geometries at various eccentricity factors.

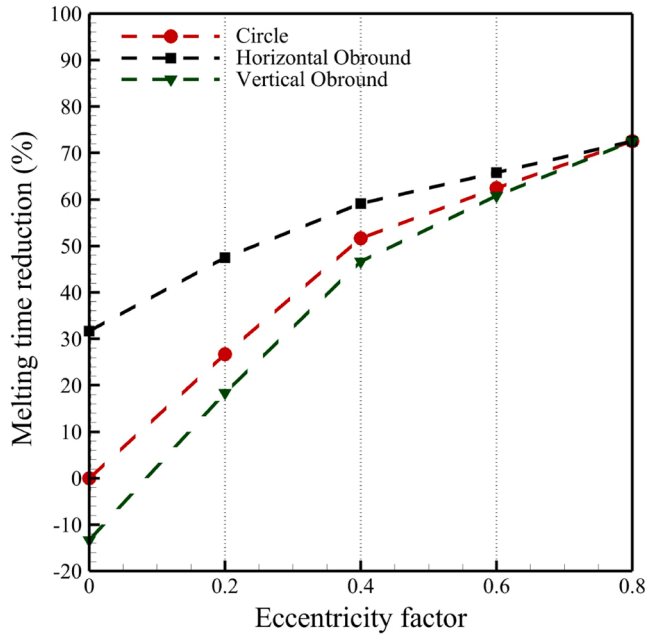

Fig. 16. Comparison of melting time reduction for different shell geometries at various eccentricity factors.

the vertical obround shell decrease by 14 %, 19 %, 15 %, and 10 % compared to the circular shell under the same eccentricity factors. However, at an eccentricity of 0.8, no significant difference in the time-averaged heat transfer rate is observed among all geometries. Fig. 19 shows the variation of time-averaged heat transfer rate improvement with eccentricity factor for the different shell configurations. Time-averaged heat transfer rate improvement quantifies the enhancement in time-averaged heat transfer rate in comparison to the concentric circular shell, which is considered the base case. It is evident that the horizontal obround shell outperforms the concentric circular shell (base case) in terms of time-averaged heat transfer rate improvement at eccentricity factors of 0, 0.2, 0.4, and 0.6, with enhancements of 38 %, 77 %, 130 %, and 178 %, respectively. The time-averaged heat transfer rate improvement obtained by the vertical obround shell are 10 %, 76 %, and 139 % at eccentricity factors of 0.2, 0.4, and 0.6, respectively. However, at ec = 0, the vertical obround shell shows a 14 % reduction in time-averaged heat transfer rate improvement. It is noteworthy that for all geometries, the maximum enhancement is found to be 246 % at the largest eccentricity (ec = 0.8).

5. Experimental uncertainty analysis

The uncertainties in experimental findings are always influenced by unavoidable errors that occur during experimental measurements and depend on the uncertainty of the individual measuring instruments. The propagation of uncertainty in the final result is always influenced by the uncertainties of independent variables. Assuming that the final result (M) is determined from independent variables x_1, x_2, …, x_N, the uncertainty of the result U(M) is appropriately obtained by combining the uncertainties of the independent variables $U(x_i)$ as follows [20]:

$$M = f(x_1, x_2, \ldots, x_N) \tag{15}$$

$$U(M) = \sqrt{\sum_{i=1}^{N} \left(\frac{\partial f}{\partial x} U(x_i)\right)^2} \tag{16}$$

The maximum uncertainty values in thermal properties measurements, including specific heat capacity of solid and liquid phases, latent heat of fusion, and density in both the solid and liquid phases, were calculated to be ± 5.6 % (solid) ± 4.9 % (liquid), ± 3.1 %, and ± 1.6 % (solid) ± 1.4 % (liquid). The maximum uncertainties were found to be ± 3.4 % for liquid fraction, 8.2 % for heat transfer rate, and 11.3 % for Nusselt numbers.

6. Conclusion

The present study experimentally investigates the thermal behavior of paraffin as a PCM within shell-and-tube thermal storage units with different shell geometries heated by the inner tube at various eccentricities. Fifteen transparent latent heat storage HXs, featuring circular, horizontal, and vertical obround enclosures with various HTF tube eccentricities (0, 0.2, 0.4, 0.6, and 0.8), were examined under constant tube temperature conditions. The experimental data were used for the analysis of melt front evolution, transient liquid fraction, and heat transfer rate during the melting processes. Based on the findings, the following conclusions can be drawn:

- For all investigated shell geometries, the downward movement of the HTF tube had a significant influence on reducing the total melting time. Based on the findings, the circular, horizontal, and vertical obround shells, with an eccentricity factor of 0.8, exhibited the maximum reductions in melting time compared to the corresponding concentric tube HXs, with values of 72 %, 60 %, and 76 %, respectively.
- Compared to the concentric tube HX with circular shell (base case), the horizontal obround shell exhibited the best improvement in the melting time, with reductions of 32 %, 47 %, 59 %, and 66 % at eccentricity factors of 0, 0.2, 0.4, and 0.6, respectively.
- The time-averaged heat transfer rate and Nusselt number increase with an increase in eccentricity factor. The circular, horizontal, and vertical obround shells at an eccentricity of 0.8 demonstrated significant improvements of 246 %, 151 %, and 304 %, respectively, compared to their corresponding concentric cases.
- Among the examined geometries, the horizontal obround shell exhibited the highest enhancements in time-averaged heat transfer rates compared to the concentric circular shell (base case). Specifically, improvements of 38 %, 77 %, 130 %, and 178 % were observed at eccentricity factors of 0, 0.2, 0.4, and 0.6, respectively.

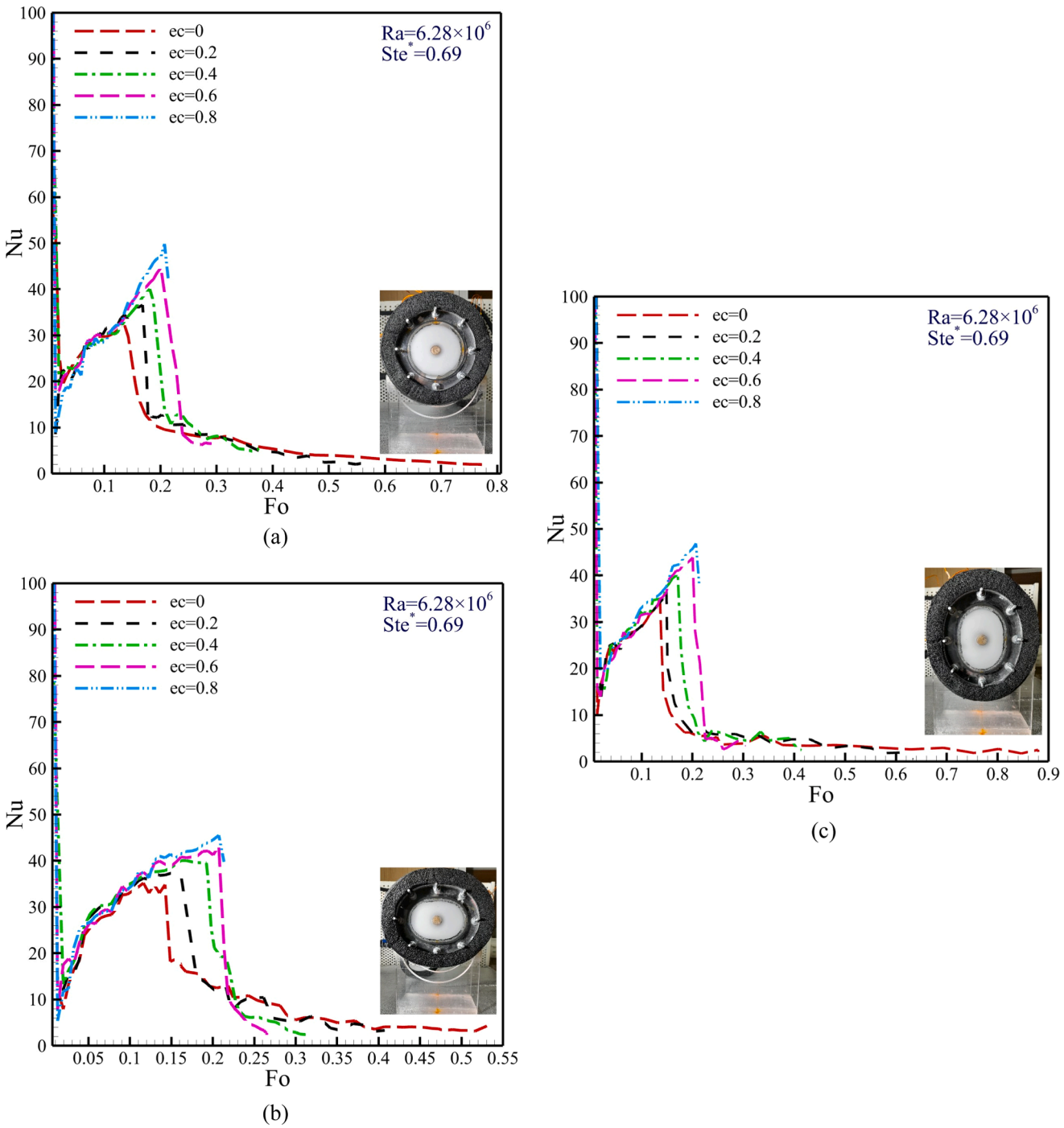

Fig. 17. Variation of Nusselt number versus Fourier number at various eccentricities for the LHS units with different shell geometries: (a) Circular shell, (b) Horizontal obround shell, (c) Vertical obround shell.

- As the eccentricity factor increased from 0 to 0.8, the difference in melting time and time-averaged heat transfer rate among the examined shell geometries decreased and became negligible at an eccentricity factor of 0.8.

CRediT authorship contribution statement

Nazila Parsa: Software, Investigation, Formal analysis, Visualization, Writing – original draft, Methodology, Validation, Writing – review & editing. **Babak Kamkari:** Conceptualization, Methodology, Resources, Supervision, Writing – review & editing. **Hossein Abolghasemi:** Supervision, Writing – review & editing, Project administration.

Declaration of competing interest

The authors declare that they have no known competing financial interests or personal relationships that could have appeared to influence the work reported in this paper.

Data availability

Data will be made available on request.

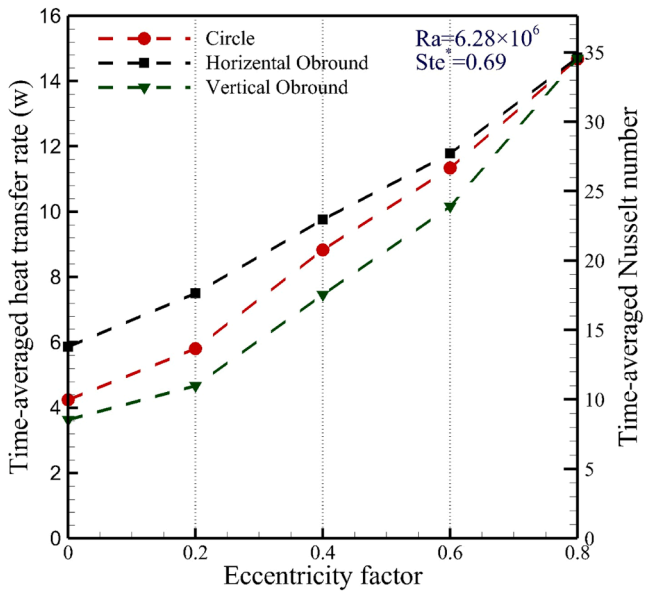

Fig. 18. Variation of time-averaged heat transfer rates and Nusselt number with eccentricity factor for different shell geometries.

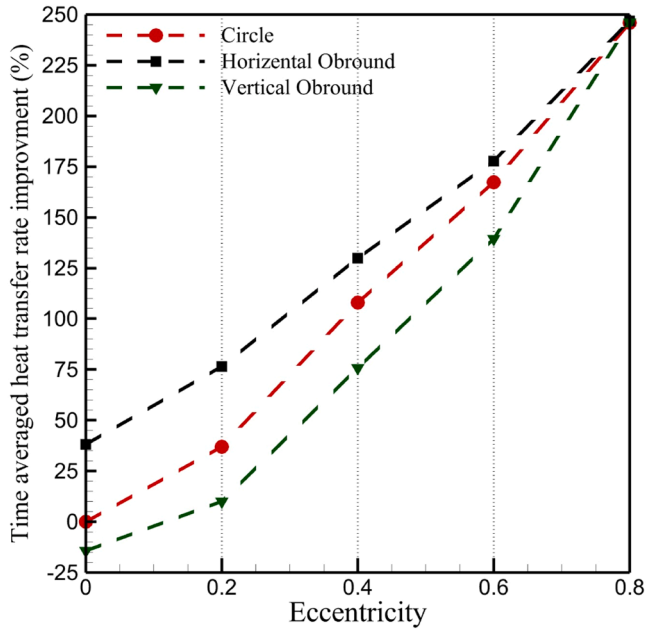

Fig. 19. Variation of time-averaged heat transfer rates improvement with eccentricity factor for different shell geometries.

References

[1] W.W. Wang, K. Zhang, L.B. Wang, Y.L. He, Numerical study of the heat charging and discharging characteristics of a shell-and-tube phase change heat storage unit, Appl. Therm. Eng. 58 (2013) 542–553, https://doi.org/10.1016/j.applthermaleng.2013.04.063.

[2] G.S. Sodhi, A.K. Jaiswal, K. Vigneshwaran, P. Muthukumar, Investigation of charging and discharging characteristics of a horizontal conical shell and tube latent thermal energy storage device, Energy Convers. Manag. 188 (2019) 381–397, https://doi.org/10.1016/j.enconman.2019.03.022.

[3] R. Karami, B. Kamkari, Experimental investigation of the effect of perforated fins on thermal performance enhancement of vertical shell and tube latent heat energy storage systems, Energy Convers. Manag. 210 (2020) 112679, https://doi.org/10.1016/j.enconman.2020.112679.

[4] H.B. Mahood, M.S. Mahdi, A.A. Monjezi, A.A. Khadom, A.N. Campbell, Numerical investigation on the effect of fin design on the melting of phase change material in a horizontal shell and tube thermal energy storage, J. Energy Storage. 29 (2020) 101331, https://doi.org/10.1016/j.est.2020.101331.

[5] A.M. Abdulateef, M. Jaszczur, Q. Hassan, R. Anish, H. Niyas, K. Sopian, J. Abdulateef, Enhancing the melting of phase change material using a fins – nanoparticle combination in a triplex tube heat exchanger, J. Energy Storage. 35 (2021) 102227, https://doi.org/10.1016/j.est.2020.102227.

[6] J. Guo, Z. Liu, B. Yang, X. Yang, J. Yan, Melting assessment on the angled fin design for a novel latent heat thermal energy storage tube, Renew. Energy. 183 (2022) 406–422, https://doi.org/10.1016/j.renene.2021.11.007.

[7] J.M. Mahdi, E.C. Nsofor, Solidification enhancement of PCM in a triplex-tube thermal energy storage system with nanoparticles and fins, Appl. Energy. 211 (2018) 975–986, https://doi.org/10.1016/j.apenergy.2017.11.082.

[8] C. Nie, J. Liu, S. Deng, Effect of geometry modification on the thermal response of composite metal foam/phase change material for thermal energy storage, Int. J. Heat Mass Transf. 165 (2021) 120652, https://doi.org/10.1016/j.ijheatmasstransfer.2020.120652.

[9] S. Seddegh, S.S.M. Tehrani, X. Wang, F. Cao, R.A. Taylor, Comparison of heat transfer between cylindrical and conical vertical shell-and-tube latent heat thermal energy storage systems, Appl. Therm. Eng. 130 (2018) 1349–1362, https://doi.org/10.1016/j.applthermaleng.2017.11.130.

[10] M. Ghalambaz, S.A.M. Mehryan, A. Veismoradi, M. Mahdavi, I. Zahmatkesh, Z. Kazemi, O. Younis, M. Ghalambaz, A.J. Chamkha, Melting process of the nano-enhanced phase change material (NePCM) in an optimized design of shell and tube thermal energy storage (TES): taguchi optimization approach, Appl. Therm. Eng. 193 (2021) 116945, https://doi.org/10.1016/j.applthermaleng.2021.116945.

[11] B. Kamkari, H. Shokouhmand, F. Bruno, Experimental investigation of the effect of inclination angle on convection-driven melting of phase change material in a rectangular enclosure, Int. J. Heat Mass Transf. 72 (2014) 186–200, https://doi.org/10.1016/j.ijheatmasstransfer.2014.01.014.

[12] S. Shi, J. Niu, Z. Wu, S. Luo, X. Gao, Y. Fang, Z. Zhang, Experimental and numerical investigation on heat transfer enhancement of vertical triplex tube heat exchanger with fractal fins for latent thermal energy storage, Int. J. Heat Mass Transf. 198 (2022) 123386, https://doi.org/10.1016/j.ijheatmasstransfer.2022.123386.

[13] X. Luo, J. Gu, H. Ma, Y. Xie, A. Li, J. Wang, Numerical study on enhanced melting heat transfer of PCM by the combined fractal fins, J. Energy Storage. 45 (2022) 103780, https://doi.org/10.1016/j.est.2021.103780.

[14] B. Kamkari, H. Shokouhmand, Experimental investigation of phase change material melting in rectangular enclosures with horizontal partial fins, Int. J. Heat Mass Transf. 78 (2014) 839–851, https://doi.org/10.1016/j.ijheatmasstransfer.2014.07.056.

[15] Y. Huang, D. Cao, D. Sun, X. Liu, Experimental and numerical studies on the heat transfer improvement of a latent heat storage unit using gradient tree-shaped fins, Int. J. Heat Mass Transf. 182 (2022) 121920, https://doi.org/10.1016/j.ijheatmasstransfer.2021.121920.

[16] Y. Shen, A.R. Mazhar, P. Zhang, S. Liu, Structure optimization of tree-shaped fins for improving the thermodynamic performance in latent heat storage, Int. J. Therm. Sci. 184 (2023) 1–13, https://doi.org/10.1016/j.ijthermalsci.2022.108003.

[17] L. Darvishvand, V. Safari, B. Kamkari, M. Alamshenas, M. Afrand, Machine learning-based prediction of transient latent heat thermal storage in finned enclosures using group method of data handling approach: a numerical simulation, Eng. Anal. Bound. Elem. 143 (2022) 61–77, https://doi.org/10.1016/j.enganabound.2022.06.009.

[18] V. Safari, H. Abolghasemi, L. Darvishvand, B. Kamkari, Thermal performance investigation of concentric and eccentric shell and tube heat exchangers with different fin configurations containing phase change material, J. Energy Storage. 37 (2021) 102458, https://doi.org/10.1016/j.est.2021.102458.

[19] V. Safari, B. Kamkari, K. Hooman, J.M. Khodadadi, Sensitivity analysis of design parameters for melting process of lauric acid in the vertically and horizontally oriented rectangular thermal storage units, Energy 255 (2022) 124521, https://doi.org/10.1016/j.energy.2022.124521.

[20] V. Safari, B. Kamkari, N. Hewitt, K. Hooman, Experimental comparative study on thermal performance of latent heat storage tanks with pin, perforated, and rectangular fins at different orientations, Therm. Sci. Eng. Prog. 48 (2024) 102401, https://doi.org/10.1016/j.tsep.2024.102401.

[21] Z.A. Qureshi, E. Elnajjar, O. Al-Ketan, R.A. Al-Rub, S.B. Al-Omari, Heat transfer performance of a finned metal foam-phase change material (FMF-PCM) system incorporating triply periodic minimal surfaces (TPMS), Int. J. Heat Mass Transf. 170 (2021) 121001, https://doi.org/10.1016/j.ijheatmasstransfer.2021.121001.

[22] Z.N. Meng, P. Zhang, Experimental and numerical investigation of a tube-in-tank latent thermal energy storage unit using composite PCM, Appl. Energy. 190 (2017) 524–539, https://doi.org/10.1016/j.apenergy.2016.12.163.

[23] H. Nabilou, K. Gharali, S. Ebadi, S.Maleki Dastjerdi, Application of partial wire mesh and particle image velocimetry for rectangular phase change material containers as efficient thermal energy storage systems, Energy Sci. Eng. 10 (2022) 973–992, https://doi.org/10.1002/ese3.1079.

[24] Y.C. Weng, H.P. Cho, C.C. Chang, S.L. Chen, Heat pipe with PCM for electronic cooling, Appl. Energy. 88 (2011) 1825–1833, https://doi.org/10.1016/j.apenergy.2010.12.004.

[25] A. Ebrahimi, M.J. Hosseini, A.A. Ranjbar, M. Rahimi, R. Bahrampoury, Melting process investigation of phase change materials in a shell and tube heat exchanger enhanced with heat pipe, Renew. Energy. 138 (2019) 378–394, https://doi.org/10.1016/j.renene.2019.01.110.

[26] V.S. Vigneswaran, G. Kumaresan, B.V. Dinakar, K.K. Kamal, R. Velraj, Augmenting the productivity of solar still using multiple PCMs as heat energy storage, J. Energy Storage. 26 (2019) 101019, https://doi.org/10.1016/j.est.2019.101019.

[27] L. Kalapala, J.K. Devanuri, Influence of operational and design parameters on the performance of a PCM based heat exchanger for thermal energy storage – A review, J. Energy Storage. 20 (2018) 497–519, https://doi.org/10.1016/j.est.2018.10.024.
[28] M. Ashiq, R. Francisco, M.B.S. Kumar, Enhancement of heat transfer in paraffin wax PCM using nano graphene composite for industrial helmets, J. Energy Storage. 26 (2019) 100982, https://doi.org/10.1016/j.est.2019.100982.
[29] M. Parsazadeh, X. Duan, Numerical study on the effects of fins and nanoparticles in a shell and tube phase change thermal energy storage unit, Appl. Energy. 216 (2018) 142–156, https://doi.org/10.1016/j.apenergy.2018.02.052.
[30] S.F. Hosseinizadeh, A.A.R. Darzi, F.L. Tan, Numerical investigations of unconstrained melting of nano-enhanced phase change material (NEPCM) inside a spherical container, Int. J. Therm. Sci. 51 (2012) 77–83, https://doi.org/10.1016/j.ijthermalsci.2011.08.006.
[31] Y. Lin, Y. Jia, G. Alva, G. Fang, Review on thermal conductivity enhancement, thermal properties and applications of phase change materials in thermal energy storage, Renew. Sustain. Energy Rev. 82 (2018) 2730–2742, https://doi.org/10.1016/j.rser.2017.10.002.
[32] B. Kamkari, H.J. Amlashi, Numerical simulation and experimental verification of constrained melting of phase change material in inclined rectangular enclosures, Int. Commun. Heat Mass Transf. 88 (2017) 211–219, https://doi.org/10.1016/j.icheatmasstransfer.2017.07.023.
[33] M.A. Alnakeeb, W.M. Galal, M.E. Youssef, M.M. Sorour, Melting characteristics of concentric and eccentric inner elliptic tube in double tube latent heat energy storage unit, Alexandria Eng. J. 73 (2023) 443–460, https://doi.org/10.1016/j.aej.2023.05.001.
[34] S. Jain, K.Ravi Kumar, D. Rakshit, B. Premachandran, K.S. Reddy, Study on the melting dynamics of latent heat storage for various orientations, shell shapes, and eccentricity, Therm. Sci. Eng. Prog. 45 (2023) 102087, https://doi.org/10.1016/j.tsep.2023.102087.
[35] M. Yusuf Yazici, M. Avci, O. Aydin, M. Akgun, Effect of eccentricity on melting behavior of paraffin in a horizontal tube-in-shell storage unit: an experimental study, Sol. Energy. 101 (2014) 291–298, https://doi.org/10.1016/j.solener.2014.01.007.
[36] V. Safari, B. Kamkari, H. Abolghasemi, Investigation of the effects of shell geometry and tube eccentricity on thermal energy storage in shell and tube heat exchangers, J. Energy Storage. 52 (2022) 104978, https://doi.org/10.1016/j.est.2022.104978.
[37] Y. Pahamli, M.J. Hosseini, A.A. Ranjbar, R. Bahrampoury, Analysis of the effect of eccentricity and operational parameters in PCM-filled single-pass shell and tube heat exchangers, Renew. Energy. 97 (2016) 344–357, https://doi.org/10.1016/j.renene.2016.05.090.
[38] Y. Xu, Z. Zheng, S. Chen, X. Cai, C. Yang, Parameter analysis and fast prediction of the optimum eccentricity for a latent heat thermal energy storage unit with phase change material enhanced by porous medium, Appl. Therm. Eng. 186 (2021) 116485, https://doi.org/10.1016/j.applthermaleng.2020.116485.
[39] M.A. Alnakeeb, M.A. Abdel Salam, M.A. Hassab, Eccentricity optimization of an inner flat-tube double-pipe latent-heat thermal energy storage unit, Case Stud, Therm. Eng. 25 (2021) 100969, https://doi.org/10.1016/j.csite.2021.100969.
[40] Z. Zheng, Y. Xu, M. Li, Eccentricity optimization of a horizontal shell-and-tube latent-heat thermal energy storage unit based on melting and melting-solidifying performance, Appl. Energy. 220 (2018) 447–454, https://doi.org/10.1016/j.apenergy.2018.03.126.
[41] N.S. Dhaidan, J.M. Khodadadi, T.A. Al-Hattab, S.M. Al-Mashat, Experimental and numerical investigation of melting of NePCM inside an annular container under a constant heat flux including the effect of eccentricity, Int. J. Heat Mass Transf. 67 (2013) 455–468, https://doi.org/10.1016/j.ijheatmasstransfer.2013.08.002.
[42] M. Faghani, M.J. Hosseini, R. Bahrampoury, Numerical simulation of melting between two elliptical cylinders, Alexandria Eng. J. 57 (2018) 577–586, https://doi.org/10.1016/j.aej.2017.02.003.
[43] I.G. Demirkiran, E. Cetkin, Emergence of rectangular shell shape in thermal energy storage applications : fitting melted phase changing material in a fixed space, Energy Storage J 37 (2021) 102455, https://doi.org/10.1016/j.est.2021.102455.
[44] M.S. Mahdi, A.A. Khadom, H.B. Mahood, A.N. Campbell, Numerical Study of Latent Heat Storage Unit Thermal Performance Enhancement Using Natural Inspired Fins, in: IOP Conf. Ser. Mater. Sci. Eng. 1076, 2021 012028, https://doi.org/10.1088/1757-899x/1076/1/012028.
[45] H. Shokouhmand, B. Kamkari, Experimental investigation on melting heat transfer characteristics of lauric acid in a rectangular thermal storage unit, Exp. Therm. Fluid Sci. 50 (2013) 201–212, https://doi.org/10.1016/j.expthermflusci.2013.06.010.
[46] W.B. Ye, M. Arıcı, 3D validation, 2D feasibility, corrected and developed correlations for pure solid-gallium phase change modeling by enthalpy-porosity methodology, Int. Commun. Heat Mass Transf. 144 (2023) 106780, https://doi.org/10.1016/j.icheatmasstransfer.2023.106780.
[47] M. Avci, M.Y. Yazici, Experimental study of thermal energy storage characteristics of a paraffin in a horizontal tube-in-shell storage unit, Energy Convers. Manag. 73 (2013) 271–277, https://doi.org/10.1016/j.enconman.2013.04.030.
[48] A.A.R. Darzi, M. Farhadi, K. Sedighi, Numerical study of melting inside concentric and eccentric horizontal annulus, Appl. Math. Model. 36 (2012) 4080–4086, https://doi.org/10.1016/j.apm.2011.11.033.
[49] Y. Harmen, Y. Chhiti, M. El Fiti, M. Salihi, C. Jama, Eccentricity analysis of annular multi-tube storage unit with phase change material, J. Energy Storage. 64 (2023) 107211, https://doi.org/10.1016/j.est.2023.107211.
[50] X. Cao, Y. Yuan, B. Xiang, F. Highlight, Effect of natural convection on melting performance of eccentric horizontal shell and tube latent heat storage unit, Sustain. Cities Soc. 38 (2018) 571–581, https://doi.org/10.1016/j.scs.2018.01.025.